Supporting Information

Unveiling Nanopore-Confined Crystallization and Coordination/De-coordination Mechanisms of Quinone Molecules for Ultrahigh-Rate and Ultralong-Cyclability Aqueous Zinc-Organic Batteries

Shuo Meng, Ting He*, Lu Chen, Kexuan Liao, Hang Lu, Tingting Liu, Ruijin Meng, Jie Ma, Chi Zhang* and Jinhu Yang*

Experimental Section

Chemicals and Materials. $(CH_3COO)_2Zn{\cdot}2H_2O$, 2-methylimidazole, tetramethyl-benzoquinone (TMBQ), tetrachloro-benzoquinone (TCBQ), dichloromethane (DCM), HCl were purchased from Aladdin Biological Technology Co, Ltd, China. KOH, ethanol was purchased from Adamas Reagent Ltd., China. All chemicals were used as received without further purification.

Preparation of ZIF-8 materials. For the synthesis of ZIF-8, 3 g of zinc acetate dihydrate was dispersed in 100 mL water to form a clear solution, 11.5 g of 2-methylimidazole was dissolved in 100 mL deionized water at room temperature. Then the solution of 2-MeIm was subsequently poured into the solution of zinc acetate dihydrate. After the solutions was mixed and stirred for 24 h at room temperature, the

white precipitates were centrifuged and washed with ethanol several times and dried at 60 °C.

Synthesis of the MCN and KMCN. The ZIF-8 was placed in a tube furnace, heated to 900 °C with a ramp rate of 5 °C·min^{-1}, and kept for 2 h under an argon atmosphere. The obtained black powders were washed with 1 M hydrochloric acid at room temperature for 10 min to remove the residual Zn species on its surface, yielding the MOF-derived carbon nanocage (MCN) polyhedrons. Then, the MCN was mixed with KOH at a mass ratio of 1:2 and activated at 800 °C for 2 h under an argon atmosphere. After cooling to room temperature, the products were treated with 1 M hydrochloric acid, washed by deionized water to pH ≈ 7, and vacuum dried overnight at 80 °C, the KOH activated MOF-derived carbon nanocage (KMCN) was obtained. To explore the effect of KOH activation we synthesized other mass ratio, 1:1 and 1:3, the obtained activated materials were named as KMCN-L and KMCN-H, respectively.

Synthesis of the TMBQ@KMCN and TCBQ@KMCN composites. In a typical process, the KMCN was placed in a Schlenk tube and vacuumed at 140 °C for several hours. Then, the reaction tube was cooled down to room temperature under vacuuming. Afterwards the dichloromethane solution of TMBQ (600mg mL^{-1}) was injected into the Schlenk tube completely to immerse the KMCN powder. The mixture was sonicated for 30 min and then stirred for 12 h at room temperature. Finally, the mixture was filtered through ethanol to clean the excess TMBQ and dried in an oven at 50 °C for 30 min. In addition, we also employed the same method to prepare TCBQ-impregnated KMCN (TCBQ@KMCN). For comparison, we used the similar method except without

a vacuum-heating process to prepare TMBQ-impregnated KMCN (TMBQ-KMCN) with a less TMBQ loading. Besides, the mixture of TMBQ and KMCN (TMBQ/KMCN) was also prepared by grinding TMBQ and KMCN in a mortar in the presence of a small amount of ethanol.

Material Characterizations. The morphologies and microstructures were characterized by a scanning electron microscopy (SEM, Hitachi S- 4800, 3 kV) and a high-resolution transmission electron microscope (HRTEM, JEOL JEM2100F,24 200 kV) together with associated energy-dispersive X-ray spectroscopy (EDS). X-ray diffraction patterns (XRD) were obtained by using a D8 advance X-ray diffractometer with a Cu Kα radiation source (λ = 0.15418 nm) in a step of 0.02° over a 2θ range of 5−50°. X-ray photoelectron spectroscopy (XPS) investigation was conducted on PHI-5000C ESCA system (Perkin Elmer) with Mg Kα radiation and the C1s peak at 284.6 eV as internal standard. Fourier transform infrared (FTIR) spectra were recorded on Nicolet iS10 FT-IR spectrometric analyzer. Thermal gravimetric (TG) analysis was carried out on a Q600 SDT instrument (TA, USA) under N_2 atmosphere with a heating rate of 10 °C min^{-1} within a temperature range of 25 to 450 °C. N_2 adsorption-desorption isotherms were obtained by using a Micromeritics 3Flex analyzer at the testing temperature of 77 K. Before the measurements, the sample was degassed in vacuum at 180 °C for at least 8 h. The Brunauer-Emmett- Teller method was utilized to calculate the surface areas. The pore size distributions were retrieved by using the Barrett-Joyner-Halanda (BJH) method from the adsorption branch of the isotherms.

Electrochemical Measurements. The CR2032 coin-type cells were assembled at room

temperature with glass fibers (GF/D) as the separator, and zinc foil as the counter electrode. The zinc foil anode was used directly without any pretreatment. To prepare the working electrodes, active materials, Ketjen black (ECP-600JD) and carboxymethylcellulose sodium (CMC) binder were mixed with a mass ratio of 8:1:1 to forming a slurry. The slurries were also coated onto a graphite foil current collector and dried in vacuum at 40 °C. The active materials loading was about 1.6 mg cm^{-2}. For high-mass-loading tests (10.6 mg cm^{-2}) of the TMBQ@KMCN electrode, Ti foil electrodes (Ø =12 mm) were employed. The electrolyte was 2 M $ZnSO_4$ solution. The galvanostatic charge/discharge measurement was conducted on a LAND CT2001A system within a voltage window of 0.2–1.6 V under various C-rates. It is noted the theoretical capacity of the quinones was employ to set as the benchmark for battery performance tests (1 C = 326 mAg^{-1} for TMBQ, 1C = 218 mAh g^{-1} for TCBQ), considering the difficulty in precisely determining the theoretical capacity of composite materials. The cyclic voltammetry (CV) curves and electrochemical impedance spectroscopy (0.01 Hz to 100 kHz) were recorded by a CHI760E electrochemical workstation (Chenhua Instruments Co China).

Theoretical Calculation. We have employed the Vienna Ab Initio Package (VASP)[1, 2] to perform all the density functional theory (DFT) calculations within the generalized gradient approximation (GGA) using the PBE[3] formulation. We have chosen the projected augmented wave (PAW) potentials[4, 5] to describe the ionic cores and take valence electrons into account using a plane wave basis set with a kinetic energy cutoff of 520 eV. Partial occupancies of the Kohn−Sham orbitals were allowed using the

Gaussian smearing method and a width of 0.05 eV. The electronic energy was considered self-consistent when the energy change was smaller than 10^{-5} eV. A geometry optimization was considered convergent when the force change was smaller than 0.05 eV/Å. Grimme's DFT-D3 methodology[6] was used to describe the dispersion interactions. The equilibrium lattice constants of TMBQ unit cell were optimized, when using a 3×3×2 Monkhorst-Pack k-point grid for Brillouin zone sampling During structural optimizations, the gamma point in the Brillouin zone was used for k-point sampling, and all atoms were allowed to relax. The crystal structures of TMBQ were obtained from literatures.[7] Finally, when computing the migration barrier for Zn ions, due to computational limitations associated with the DFT calculations, we simplified the model by reducing the number of atoms from the normal configuration. We adopted the most elementary structure for simulating the migration barrier in order to stay within the computational capacity constraints. The TMBQ structural cluster was loaded inside the nanotube-like pore channel, forming a composite structure, and the nudged elastic band (NEB) method [8] was employed to calculate the migration barrier of Zn ions by inserting a series of Zn ions along the migration path between the initial and final states.

Calculations of the number of TMBQ molecules in the pore of KMCN. The number of TMBQ molecules per unit cubic nanometer in the saturated DCM solution was calculated as follows:

$$N_{TMBQ} = \frac{C_{TMBQ}}{M_{TMBQ}} \times \frac{1}{10^{21}} \times N_A$$

Where C_{TMBQ} is the concentration of the saturated TMBQ-DCM solution (0.6 g mL^{-1}). N_A is Avogadro's constant, which is 6.02×10^23. M_{TMBQ} is relative molecular mass of

TMBQ, which is 164 g mol^{-1}. 10^{21} serves as a conversion factor, where 1 mL equals 10^{21} nm^3. Herein, N_{TMBQ} was calculated to be 2.2 per nm^3. Considering the size of TMBQ molecule is about 0.59 nm, the solvent molecules of DCM occupy a major in the unit space of 1 nm^3.

Therefore, when the saturated TMBQ-DCM solution was impregnated in to the pore of KMCN, the number of TMBQ molecules in a cylindrical pore with a diameter of 3 nm (average pore diameter, *R*) and a length of 12 nm can be calculated using the following equation:

$$n_{TMBQ} = \pi \times (\frac{R}{2})^2 \times 12 \times N_{TMBQ}$$

Accordingly, the value of n_{TMBQ} is 187, and this implies that there are approximately 187 TMBQ molecules in each pore with 12 nm length.

Quantitative calculation of Zn^{2+} vs. proton storage in TMBQ. For more convenient calculations, we fabricated the electrode by pressing it onto a titanium mesh using a TMBQ: Ketjen black: CMC ratio of 8:1:1. Subsequently, the electrode was then discharged to its final state, and we washed the fully discharged electrode with deionized water for several minutes to remove any residual electrolyte before subsequent testing.

During the discharge process of this electrode, the following three equations apply:

$$TMBQ + Zn^{2+} \rightarrow Zn\text{-}TMBQ \quad \text{I}$$

$$TMBQ + 2H^{+} \rightarrow 2H\text{-}TMBQ \quad \text{II}$$

$$4Zn^{2+} + SO_4^{2-} + 6OH^{-} + 5H_2O \rightarrow Zn_4SO_4(OH)_6 \cdot 5H_2O \quad \text{III}$$

Therefore, at the end of the discharge state (0.2 V), the composition of the discharged cathode contains the mixture of: (1) proton inserted TMBQ (2H-TMBQ), (2) Zn^{2+}-inserted TMBQ (Zn-TMBQ), (3) $Zn_4SO_4(OH)_6{\cdot}5H_2O$ and (4) KB and CMC.

In the discharged cathode (0.2 V), It is noteworthy that zinc exists in $Zn_4SO_4(OH)_6{\cdot}5H_2O$ as well as Zn^{2+}-inserted TMBQ, and SO_4^{2-} only exists in $Zn_4SO_4(OH)_6{\cdot}5H_2O$. The weight percentage of Zn was measured by inductively coupled plasma optical emission spectroscopy (ICP-OES). And the SO_4^{2-} was extracted from the discharged cathode with dilute hydrochloric acid, and the amount was measured by ion chromatography (IC). The ICP-OES and IC analysis resulted in Zn and SO_4^{2-} weight percentages of 25.02% and 1.44% in the discharged cathode, respectively.

Based on the proportion of SO_4^{2-}, the weight ratio of the $Zn_4SO_4(OH)_6{\cdot}5H_2O$ can be calculated:

$$Zn_4SO_4(OH)_6{\cdot}5H_2O \quad wt\% \quad = \quad \frac{SO_4^{2-}\ wt\%}{\omega[SO_4^{2-}\ in\ Zn_4SO_4(OH)_6{\cdot}5H_2O]} \quad (4)$$

Here $\omega[SO_4^{2-}$ in $Zn_4SO_4(OH)_6{\cdot}5H_2O]$ is the mass fraction of SO_4^{2-} in $Zn_4SO_4(OH)_6{\cdot}5H_2O$.

$$\omega[SO_4^{2-} \text{ in } Zn_4SO_4(OH)_6{\cdot}5H_2O] = \frac{96}{65 \times 4 + 96 + 17 \times 6 + 5 \times 18} = 17.52\%$$

It can be deduced that $Zn_4SO_4(OH)_6{\cdot}5H_2O$ wt% = 8.219%.

We know that zinc exists both in $Zn_4SO_4(OH)_6 \cdot 5H_2O$ and Zn-TMBQ, and through ICP-OES testing, we have determined that the total zinc content is 25.02%. Therefore, Therefore, we can derive the following formula:

Zn-TMBQ wt% × ω[Zn in Zn-TMBQ] + $Zn_4SO_4(OH)_6 \cdot 5H_2O$ wt% × ω[Zn in $Zn_4SO_4(OH)_6 \cdot 5H_2O$] = Zn wt% = 25.02% (5)

Here Zn-TMBQ wt% is the weight percentage of Zn^{2+}-inserted TMBQ (Zn-TMBQ) in the discharged cathode; $Zn_4SO_4(OH)_6 \cdot 5H_2O$ wt% is the weight percentage of $Zn_4SO_4(OH)_6 \cdot 5H_2O$ in the discharged cathode; ω[Zn in Zn-TMBQ] is the mass fraction of Zn in Zn^{2+}-inserted TMBQ; ω[Zn in $Zn_4SO_4(OH)_6 \cdot 5H_2O$] is the mass fraction of Zn in $Zn_4SO_4(OH)_6 \cdot 5H_2O$:

$$\omega[\text{Zn in Zn-TMBQ}] = \frac{65}{65 + 164} = 28.38\%$$

$$\omega[\text{Zn in } Zn_4SO_4(OH)_6 \cdot 5H_2O] = \frac{65 \times 4}{65 \times 4 + 96 + 17 \times 6 + 5 \times 18} = 47.44\%$$

According to equation 5, we can determine that Zn-TMBQ wt% is 74.37%.

To calculate 2H-TMBQ wt%, we need to understand that in the electrode, the total mass ratio of pure TMBQ is four times the mass ratio of [KB+CMC] (slurry ratio of TMBQ: KB: CMC = 8:1:1), as follow:

$$\text{TMBQ wt\%} = \text{2H-TMBQ wt\%} \times \frac{M_w[TMBQ]}{M_w[2H - TMBQ]} + \text{Zn-TMBQ wt\%} \times \frac{M_w[TMBQ]}{M_w[Zn - TMBQ]} = 4[\text{KB + CMC}]\ \text{wt\%} \quad (6)$$

Here 2H-TMBQ wt% is the weight percentage of proton inserted TMBQ in the discharged cathode; M_w[TMBQ] is molecular weight of TMBQ, which is 164 g mol^{-1}; M_w[2H-TMBQ] is molecular weight of proton inserted TMBQ, which is 166 g mol^{-1}; M_w[Zn-TMBQ] is molecular weight of Zn^{2+} inserted TMBQ, which is 229 g mol^{-1}. Therefore, we can derive the following equation 7:

$$2H\text{-}TMBQ\ wt\% \times \frac{164}{166} + 74.37\% \times \frac{164}{229} = 4 \times [KB + CMC]\ wt\% \quad (7)$$

Since the sum of all components equals 100%, this can be represented by the following equation :

$$2H\text{-}TMBQ\ wt\% + Zn\text{-}TMBQ\ wt\% + Zn_4SO_4(OH)_6{\cdot}5H_2O\ wt\% + [KB + CMC]\ wt\% = 100\% \quad (8)$$

$$2H\text{-}TMBQ\ wt\% + 74.37\% + 8.219\% + [KB + CMC]\ wt\% = 100\%$$

$$[KB + CMC]\ wt\% = 100\% - 74.37\% - 8.219\% - 2H\text{-}TMBQ\ wt\% \quad (9)$$

By substituting the formula from equation 9 into equation 7, we obtain:

$$2H\text{-}TMBQ\ wt\% \times \frac{164}{166} + 74.37\% \times \frac{164}{229} = 4 \times [100\% - 74.37\% - 8.219\% - 2H\text{-}TMBQ\ wt\%] \quad (10)$$

Finally, we obtain: 2H-TMBQ wt% = 3.28%

The above equations result in 2H-TMBQ wt% and Zn-TMBQ wt% of 3.28% and 74.37%, respectively. Using 2H-TMBQ wt%, we can determine the weight ratio of coordinated protons in 2H-TMBQ as:

$$[H\text{ in }2H\text{-}TMBQ]\ wt\% = 2H\text{-}TMBQ\ wt\% \times \frac{M_w[2H]}{M_w[2H-TMBQ]} = 3.28\% \times \frac{2}{166} = 0.039\%$$

[Zn in Zn-TMBQ] wt% = Zn-TMBQ wt% × $\frac{M_w[Zn]}{M_w[Zn-TMBQ]}$ = 74.37% × $\frac{65}{229}$ = 21.10%

Therefore, based on the relative atomic masses of protons and Zn, we can derive the mole of inserted Zn^{2+} is 8.3 times of proton, confirming the domination of Zn^{2+} storage in TMBQ during the redox processes.

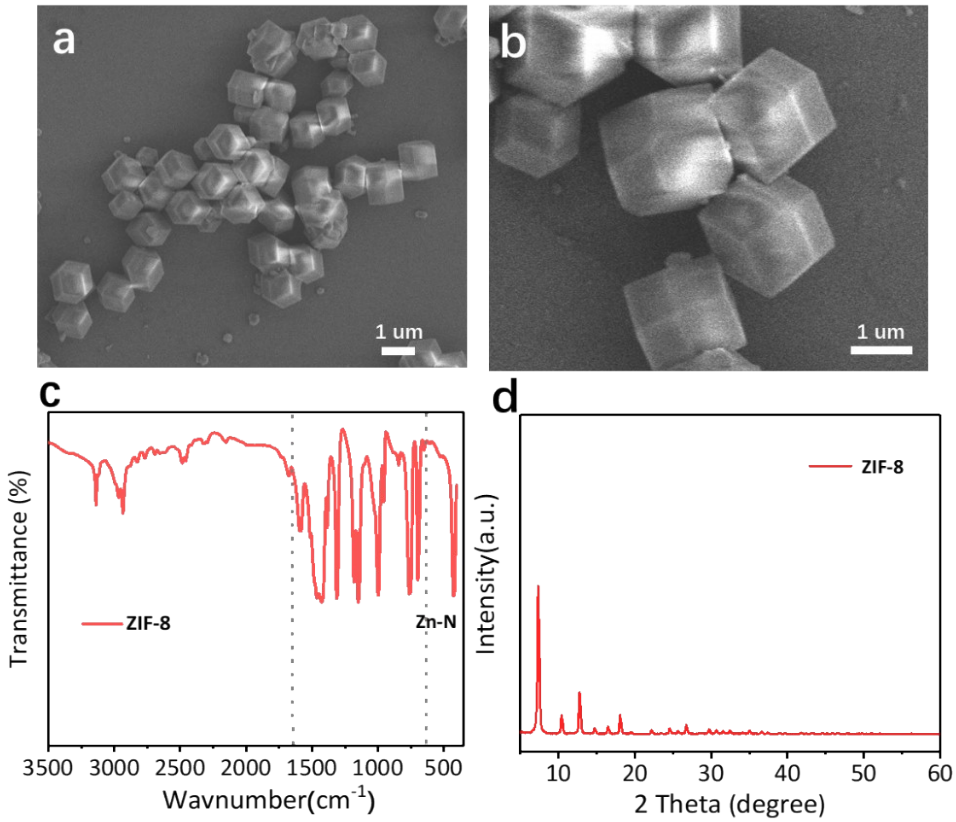

Figure S1. (a, b) SEM images of ZIF-8. (c) FTIR and (d) XRD pattern of ZIF-8.

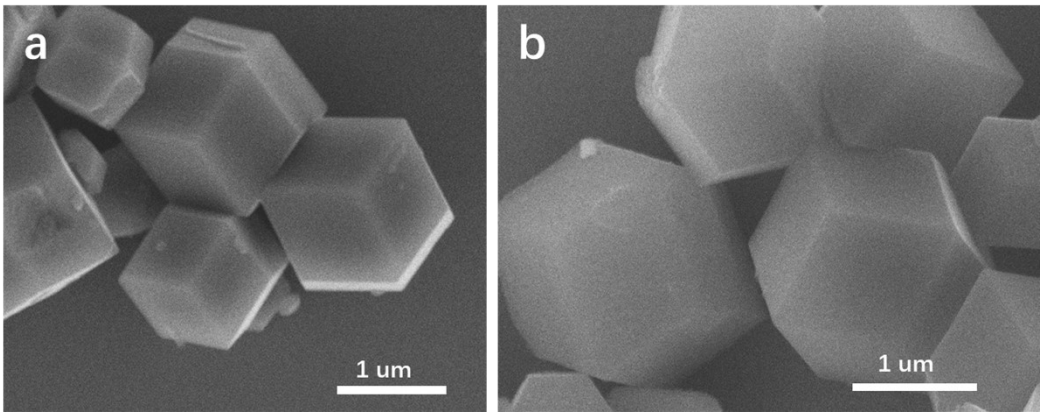

Figure S2. SEM images of (a) MCN and (b) KMCN.

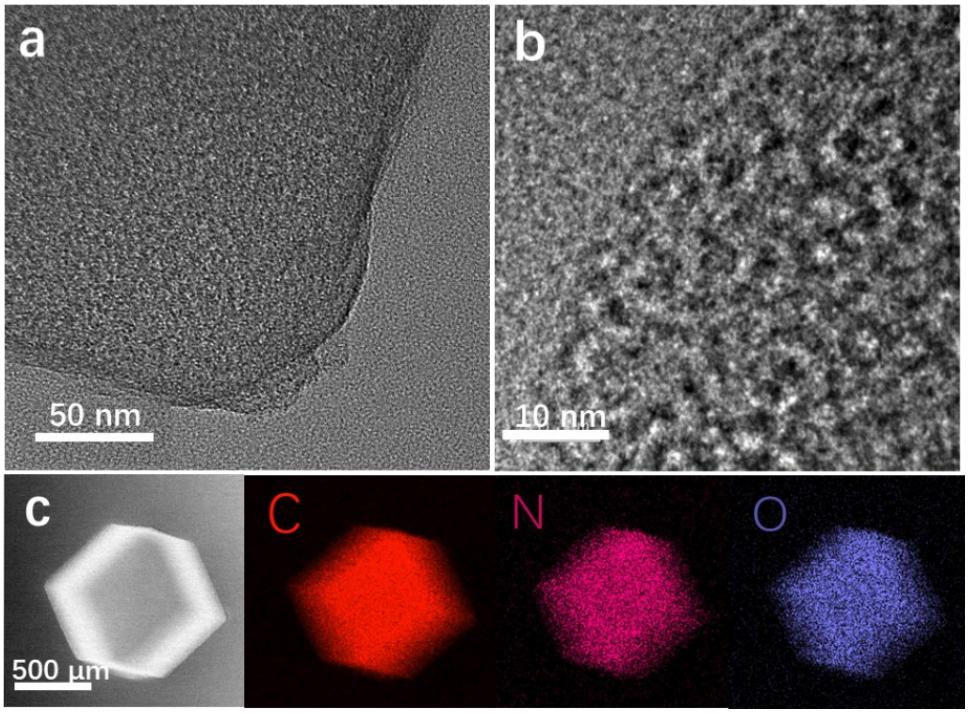

Figure S3. TEM image (a) and high-resolution TEM image (b) of the KMCN. (c) elemental mapping of the KMCN.

Note: From Figure S3a and b, abundant pore structure can be clearly observed from the TEM image. The elements of C, N and O are uniformly distributed throughout the KMCN (Figure S3c).

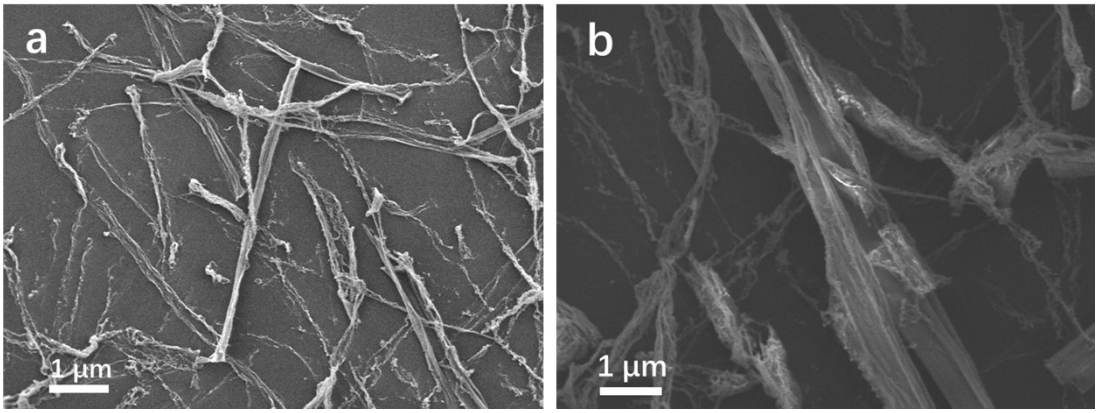

Figure S4. (a, b) SEM images of TMBQ with a fiber shape.

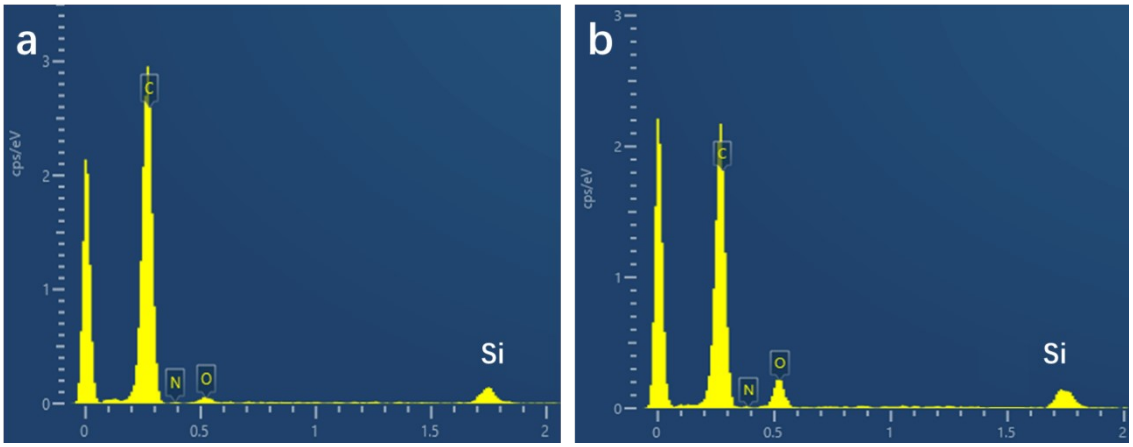

Figure S5. EDS of the KMCN (a) and TMBQ@KMCN (b).

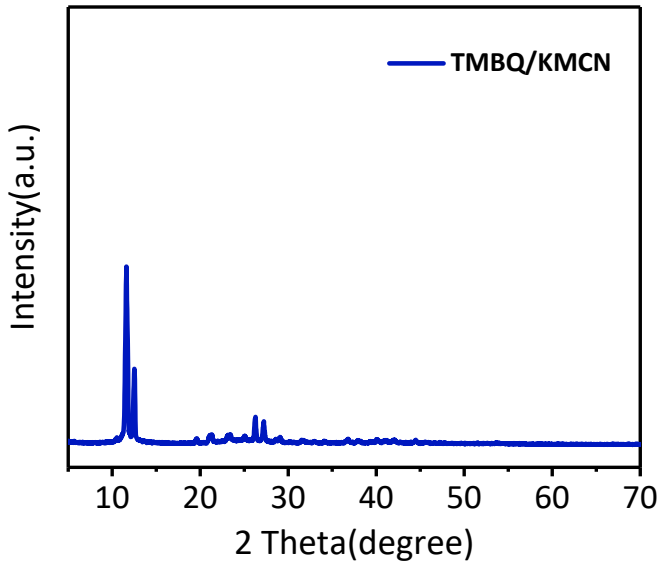

Figure S6. XRD pattern of the TMBQ/KMCN sample prepared by simply mixing of TMBQ and KMCN.

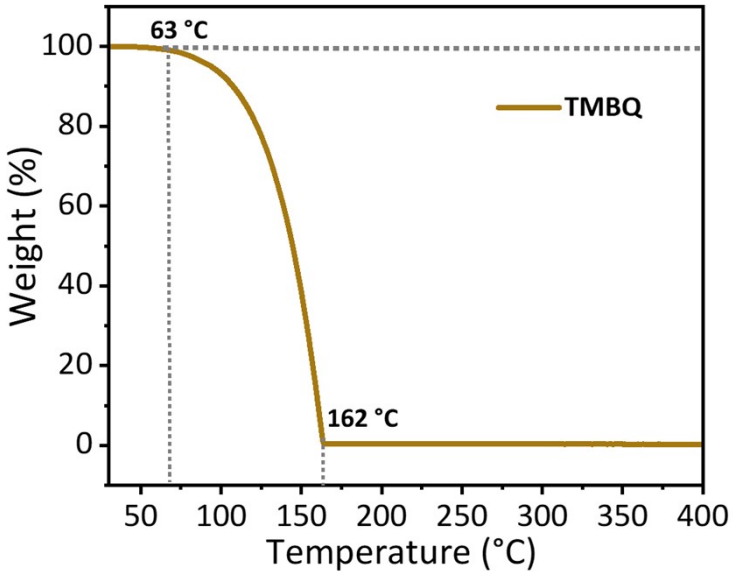

Figure S7. The TGA curve of pure TMBQ under N_2 atmosphere with the temperature ramping rate of 10 °C min^{-1}.

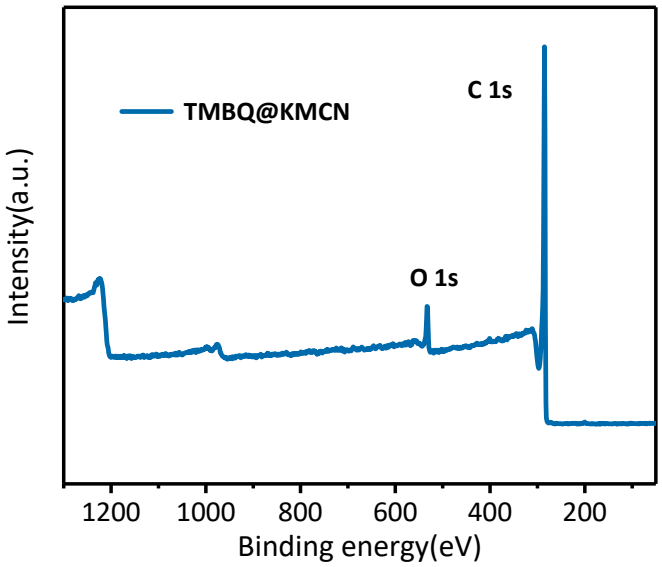

Figure S8. XPS survey spectrum of the TMBQ@KMCN.

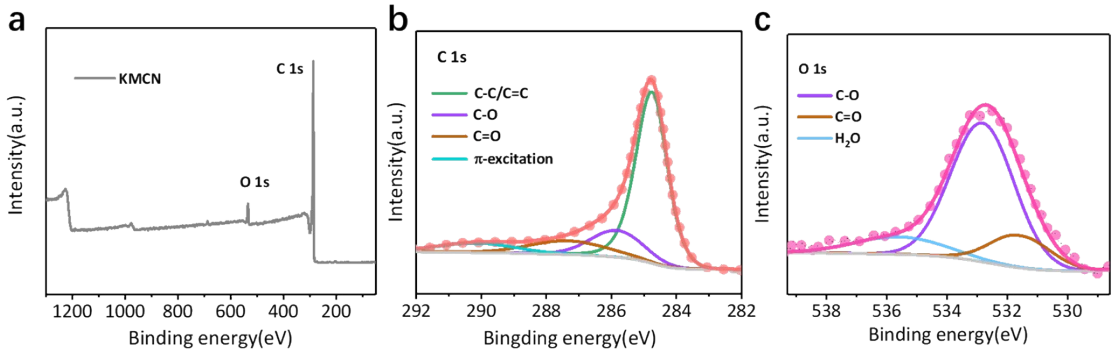

Figure S9. (a) XPS survey spectrum of the KMCN. (b, c) High-resolution C 1s and O 1s spectrum of the KMCN.

Note: In the XPS survey spectrum (Figure S9a), N element is low in intensity and not easily observed. The high-resolution C 1s spectrum exhibits four peaks at 284.8, 285.9, 287.1, and 290 eV, corresponding to the C-C/C=C, C-O, C=O, and π-excitation, respectively (Figure S9b).[9] Simultaneously, the high-resolution O 1s spectrum can be

fitted to oxygen species centered at 533.1, 531.8, and 535.5 eV, which belong to the C-O, C=O, adsorbed H_2O, respectively (Figure S9c).[9]

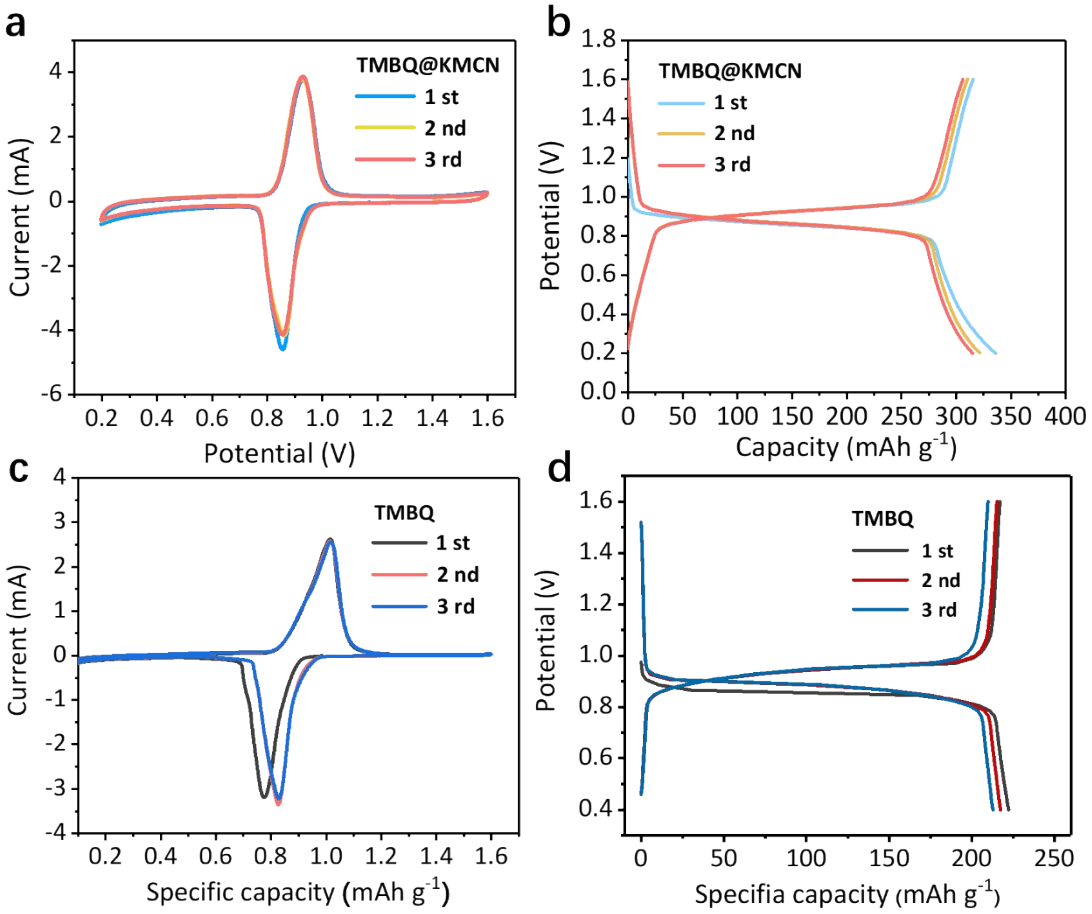

Figure S10. (a, c) CV profiles of the first three cycles for the TMBQ@KMCN and TMBQ electrodes at a scan rate 0.2 mV s^{-1}. (b, d) Voltage profles of the first three cycles for the TMBQ@KMCN and TMBQ electrodes at 0.5 C.

Note: The CV profiles of the TMBQ@KMCN electrode for the first three cycles, where the reduction and oxidation peaks appear at 0.86 and 0.93 V, respectively. Besides, the TMBQ@KMCN electrode holds a polarization voltage of 0.07 V (Figure S10a). The

cathode and anode peaks of the TMBQ electrode in the first cycle are at 0.78 V and 1.01 V, giving a polarization voltage of 0.23 V (Figure S10c). In the subsequent second and third cycle, the cathode peak shifts to the right to 0.82 V, which is due to the activation in the first cycle. This can also be observed in the charge/discharge profiles of the TMBQ electrode (Figure S10d).

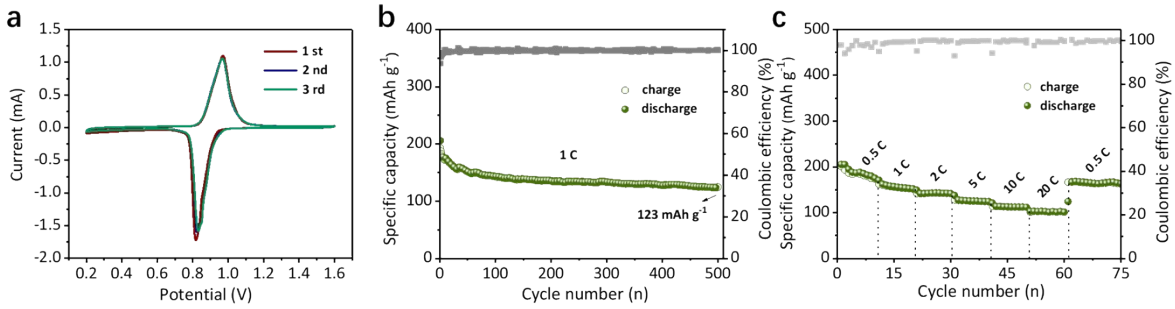

Figure S11. (a) CV profiles of the TMBQ/KMCN electrode at a scan rate of 0.2 mV s^{-1}. (b) Cycling performance of the TMBQ/KMCN electrode at 1 C. (c) Rate capability of the TMBQ/KMCN electrode from 0.5 to 20 C.

Note: From the CV curves in Figure S11a, the TMBQ/KMCN electrode shows a large polarization voltage of 0.15 V, which is larger than that of the TMBQ@KMCN electrode (0.07 V) but smaller than that of the pure TMBQ electrode (0.23 V). The TMBQ/KMCN electrode exhibits both poor cycling and rate performance (Figure S11b, c). This is due to the fact that TMBQ molecules are distributed on the surface of the KMCN, which are easy to separate and fall off into electrolyte solution, resulting a poor electrode stability.

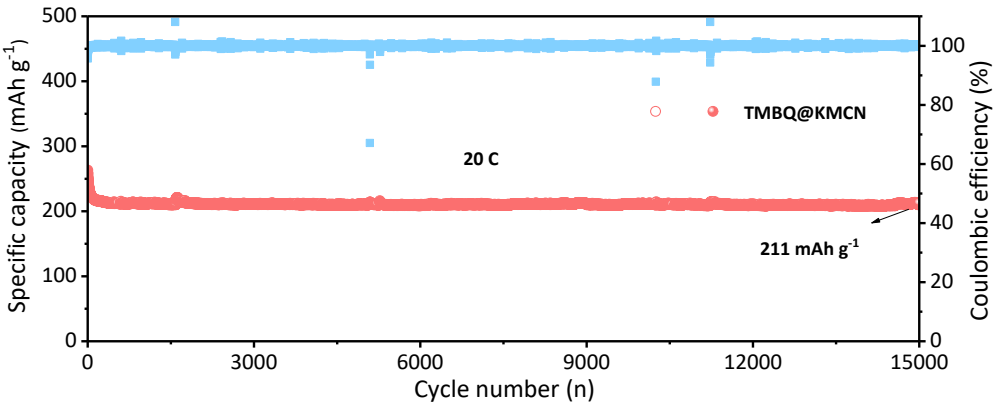

Figure S12. Long cycling test of the TMBQ@KMCN electrode at 20 C.

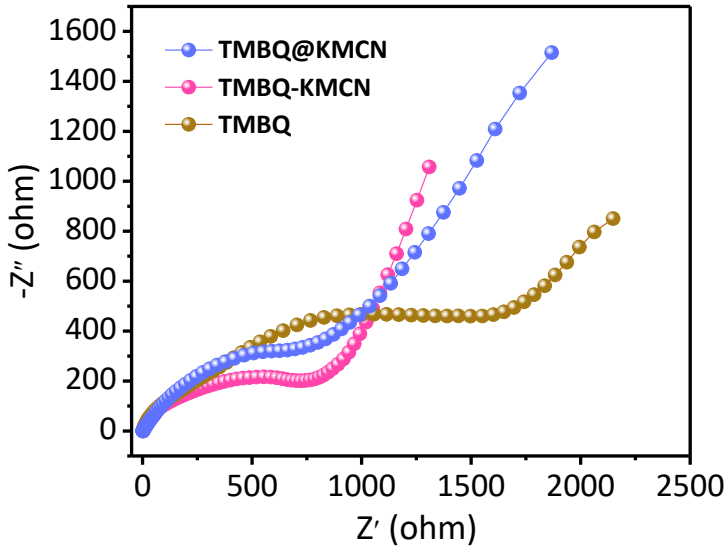

Figure S13. Nyquist plots of the TMBQ@KMCN, TMBQ-KMCN and TMBQ electrodes.

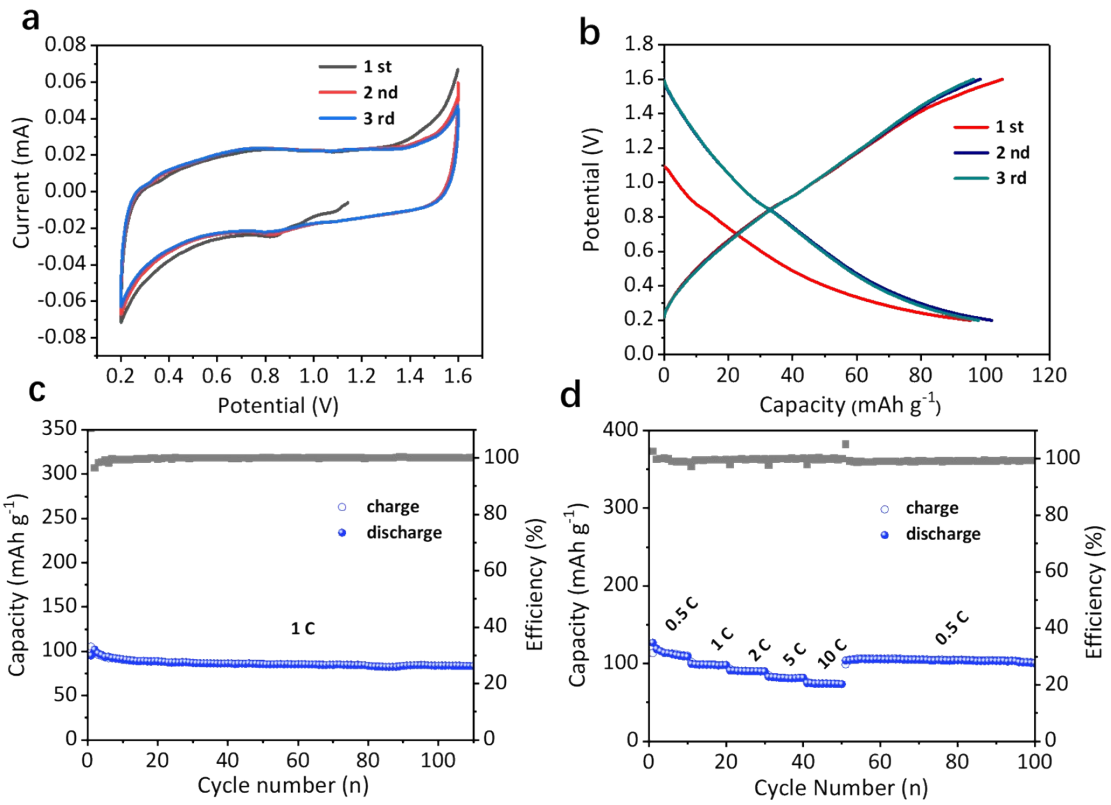

Figure S14. (a) CV profiles of the KMCN electrode at a scan rate of 0.2 mV s^{-1}. (b) Charge/discharge profles of the KMCN electrode at 1 C. (c) Cycling performance of the KMCN electrode at 1 C. (d) Rate capability of the KMCN electrode at current densities between 0.5 and 10 C.

Note: The CV profiles of the KMCN electrode show a rectangle-like shape, suggesting a distinct capacitive behavior for the KMCN during charge/discharge (Figure S14a). The charge/discharge profles of the KMCN electrode are provided in Figure S14b, where no obvious any charge/discharge plateau is found, in good agreement with the CV result. The cycling performance of the KMCN electrode at 1 C delivers a restricted capacity of 83 mAh g^{-1} after 110 cycles, exhibiting an excellent cycling stability (Figure S14c). Morever, the rate capability of KMCN electrode is shown in Figure S14d. The

reversible capacity of ≈ 112, 98, 90, 81, 74 mAh g^{-1} is achieved at 0.5, 1, 2, 5 and 10 C, respectively. When the current density returns to the initial 0.5 C after 50 cycles, a reversible capacity of 107 mAh g^{-1} can be maintained, giving rise to a high capacity retention of 95.5%. The excellent cycle stability and rate property indicate that the KMCN maintains outstanding structural stability during charging and discharging, making it suitable as a matrix for composite materials.

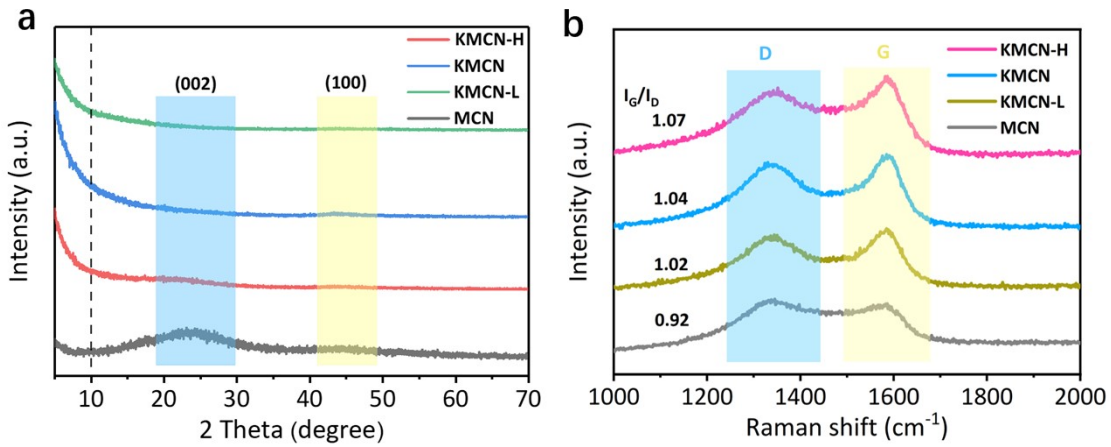

Figure S15. (a) XRD patterns and (b) Raman spectra of the MCN and KOH activated MCN with different KOH/MCN mass ratios (KMCN-L, 1:1; KMCN-H, 3:1).

Note: The influence of KOH amount during activation on pore size of the MCN was investigated. Firstly, activated MCN products were prepared with a low mass ratio of KOH/MCN (1:1, denoted as KMCN-L) and a high mass ratio (3:1, denoted as KMCN-H) which are relative to the moderate ratio (2:1) of the typical KMCN. XRD patterns of the MCN, KMCN, KMCN-L and KMCN-H reveal that all the activated samples show a strong scattering intensity at low angles with (002) peak nearly invisible (Figure

S15a), due to the highly developed pore structure within the activated samples. The Raman spectra show that the ratio of G band to the D band (I_G/I_D) increases with the rising mass ratio of KOH to MCN (Figure S15b, 0.92 increase to 1.07), indicating that the graphitization of the MCN is enhanced with the degree of KOH activation.[9]

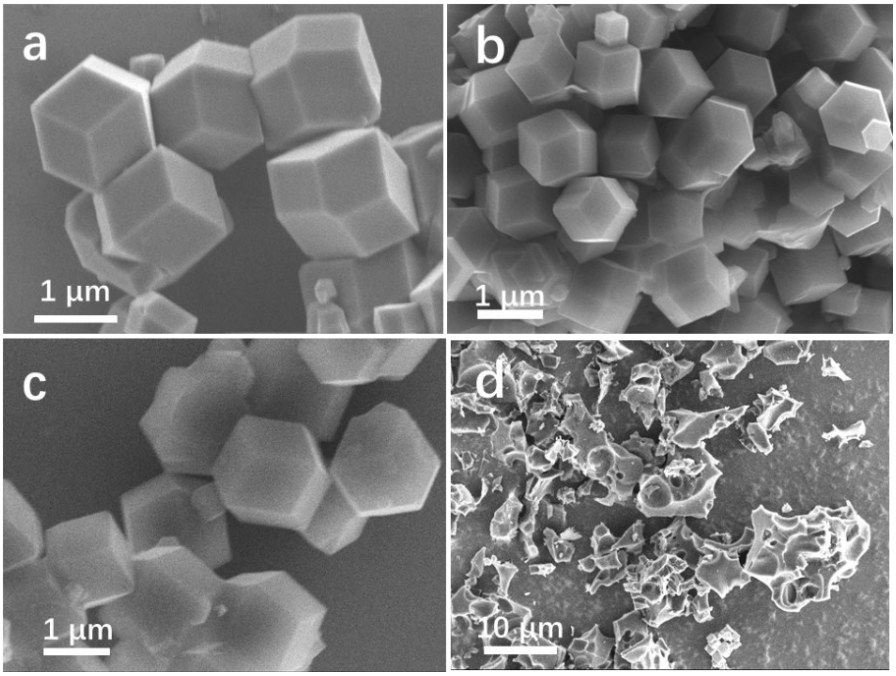

Figure S16. SEM images of the MCN (a), KMCN-L (b), KMCN (c) and KMCN-H (d).

Note: From SEM images, it is found that the MCN, KMCN and KMCN-L possess a similar rhombododecahedral morphology (Figure S16a-c), except for the KMCN-H that is fragmented due to excessive KOH etching (Figure S16d).

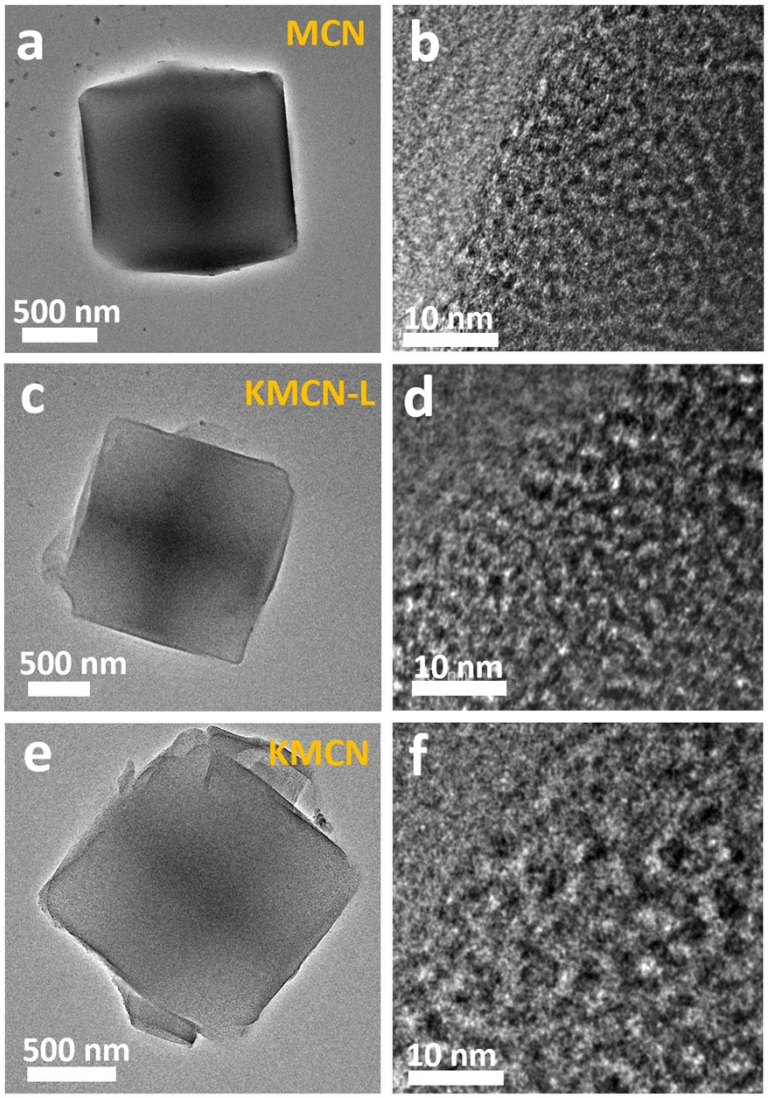

Figure S17. (a, b) TEM images of the MCN. (c, d) TEM images of the KMCN-L. (e, f) TEM images of the KMCN.

Note: From TEM images, it is evident that after KOH activation, the pore structure in all activated samples becomes richer, and the pore size increases with the increases of KOH/MCN mass ratio.

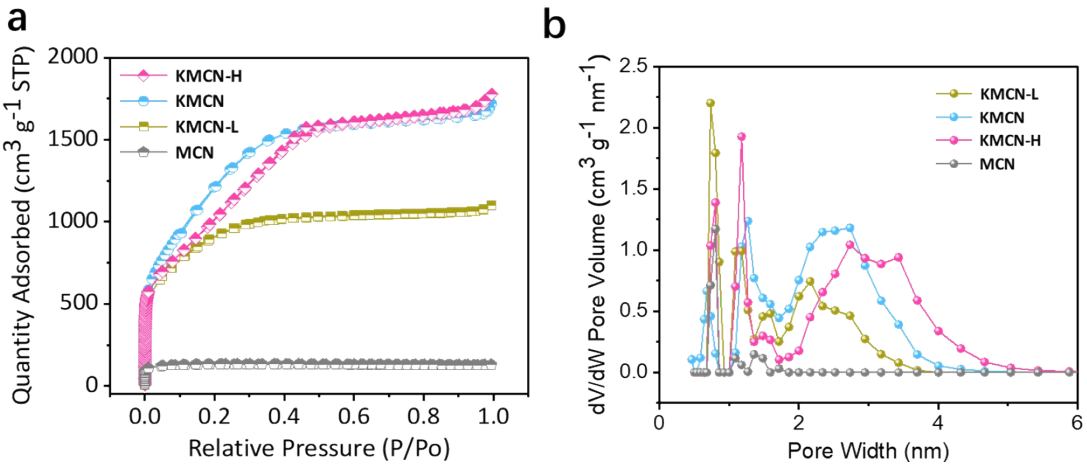

Figure S18. (a) N_2 adsorption-desorption isotherms and (b) pore-size distribution curves of the MCN and KMCN-L, KMCN, KMCN-H.

Note: MCN has a typical type-I isotherms with the concentrated micropore distribution and a limited total pore volume. And the typical type-IV isotherms are observed for the KOH-activiated samples with rapid saturation of adsorption occurs at low pressure ($P/P_0 < 0.1$) and typical H2-type hysteresis loop at P/P_0 = 0.5-0.95, proving the hierarchical porous structure and the co-existence of micro/mesoporous in activiated samples.[10] As evidenced by BET analysis, the activated samples of KMCN-L, KMCN and KMCN-H show an increased S_{BET} and V_{total} with increasing KOH/MCN mass ratio (Figure S18 and Table S4).

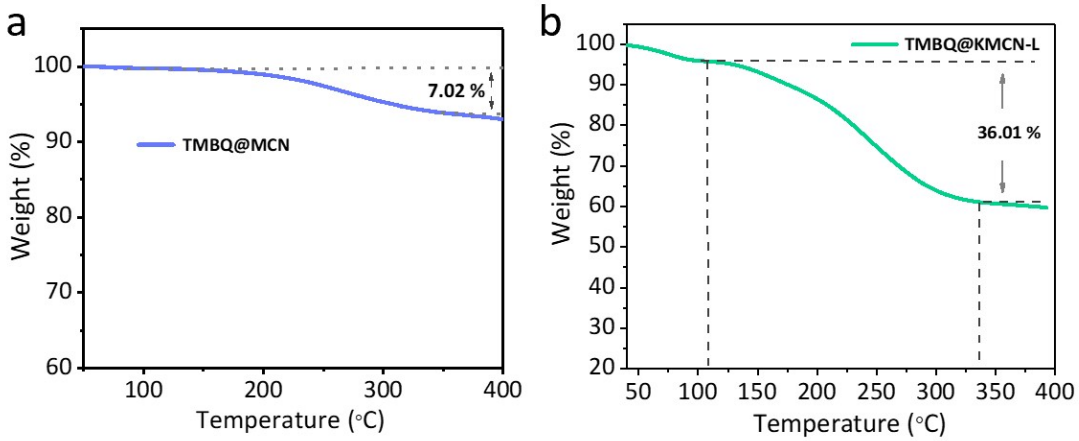

Figure S19. TGA curves of the TMBQ@MCN (a) and TMBQ@KMCN-L (b).

Note: Except for the broken KMCN-H, the MCN and KMCN-L with the intact polyhedral morphology were chosen as the matrix for TMBQ loading using the same impregnation method as the typical. The corresponding TGA data are shown in Figure S19. The weight loss before 100°C is due to the evaporation of residual fraction of solvent (ethanol *etc.*) introduced in the sample preparation. It is found that for the MCN case, only a very low TMBQ loading of 7.02% was obtained for TMBQ@MCN (Figure S19a), due to the small pore size of MCN that is difficult for efficient entrance of TMBQ. While for the case of KMCN-L, a TMBQ loading of 36.01% can be obtained (37.41 wt% at most, calculated according to the equation: $V_{KMCN\text{-}L\ total} \times C_{TMBQ} \times 100\%$, $V_{KMCN\text{-}L\ total}$ from Table S4), which is lower than that of the TMBQ@KMCN (57.22%) yet significantly higher than that of the TMBQ@MCN (Figure S19b).

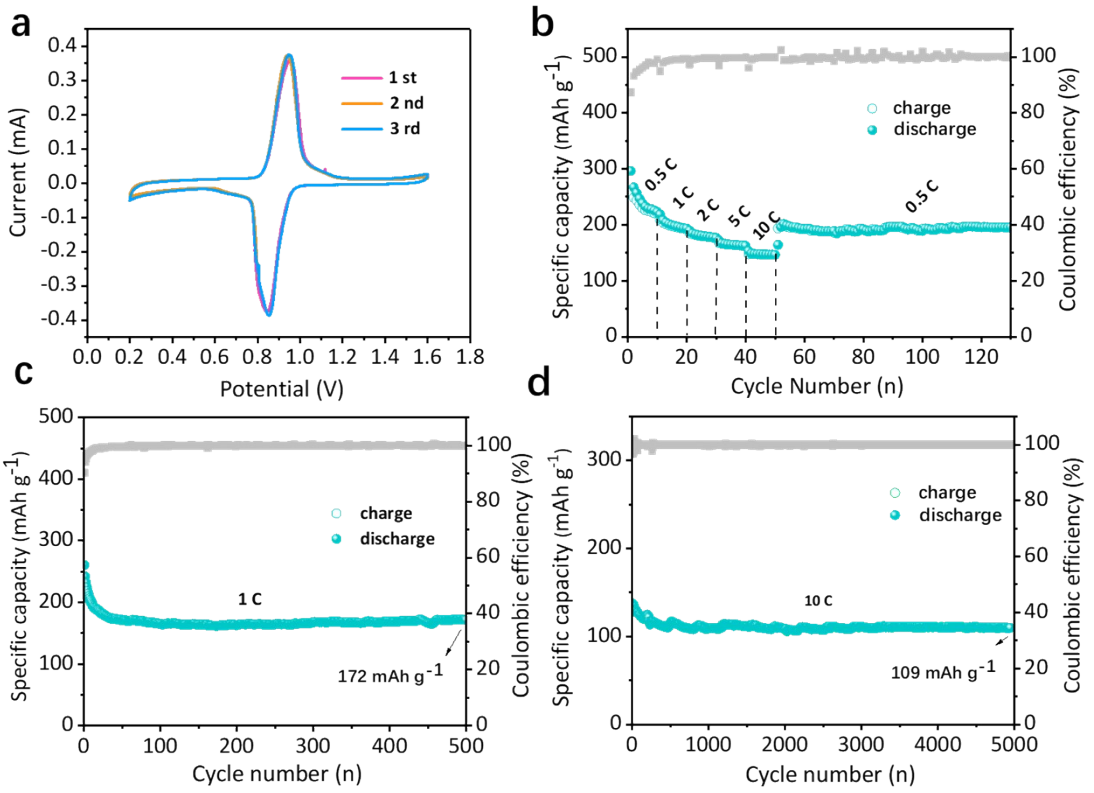

Figure S20. (a) CV curves of the TMBQ@KMCN-L at 0.2 mV s^{-1}. (b) Rate capability of the TMBQ@KMCN-L at current densities between 0.5 and 10 C. (c) Cycling performance of the TMBQ@KMCN-L at 1 C. (d) Long cycling performance of the TMBQ@KMCN-L at 10 C.

Note: The CV curves of the TMBQ@KMCN-L is similar to that of the typical TMBQ@KMCN, and they also have a lower polarization (Figure S20a). The rate capability of the TMBQ@KMCN-L is shown in Figure S20b, where the reversible capacity of ≈ 247, 198, 183, 165, 147 mAh g^{-1} is achieved at 0.5, 1, 2, 5 and 10 C, respectively. When the current goes back to the initial 0.5 C after 50 cycles, a reversible capacity of 202 mAh g^{-1} can be maintained, giving rise to a high capacity retention of 81.8%. The cycling performance of the TMBQ@KMCN-L electrode at a current

density of 1 C is shown at Figure S20c. It can be found that the TMBQ@KMCN-L electrode shows a capacity of 172 mAh g^{-1} at 1C and a Coulombic efficiency of 99.65% after 500 cycles. Furthermore, even at a higher rate of 10 C, the TMBQ@KMCN-L electrode delivers a reversible capacity of 109 mAh g^{-1} after 5000 cycles with a capacity retention of 77.8% (Figure S20d). In general, the TMBQ@KMCN-L electrode has relatively good cycling stability, yet with a lower capacity.

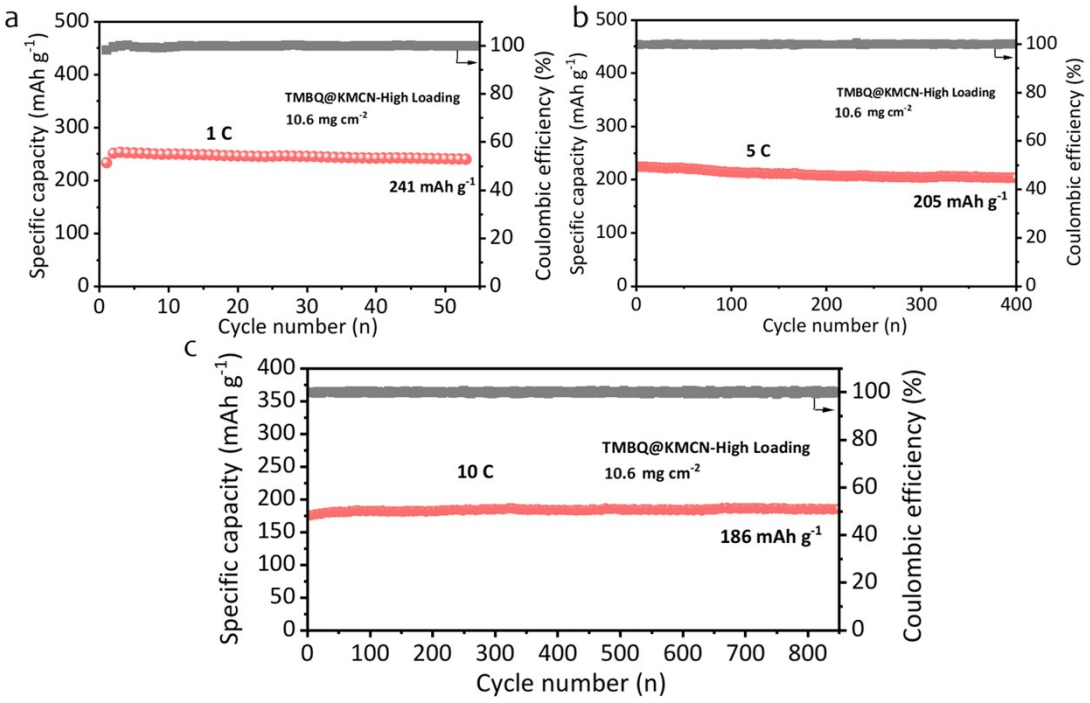

Figure S21. Cycling performance of the TMBQ@KMCN electrode with high mass loading of 10.6 mg cm^{-2} at current densities of 1 C, 5 C and 10 C.

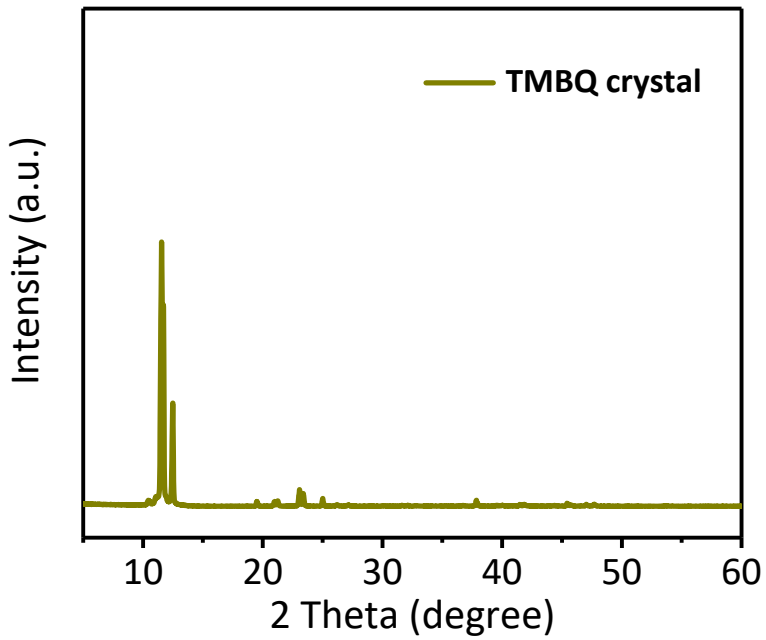

Figure S22. XRD pattern of TMBQ crystal precipitated from the saturated TMBQ-DCM solution.

Note: As the solvent DCM evaporates from the saturated TMBQ-DCM solution, TMBQ molecules gradually crystallize to form crystalline fibers with length up to several micrometers (Figure S4). It can be seen in the XRD pattern that the peaks are sharp and intensified, indicating the formation of highly crystallized products.

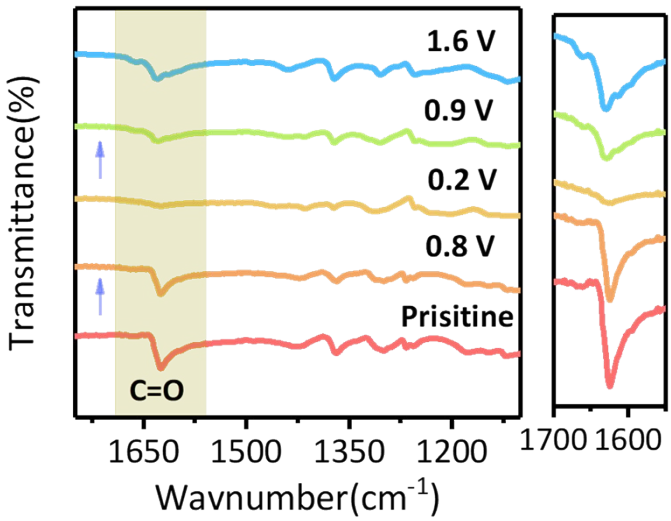

Figure S23. FTIR curves of the TMBQ@KMCN electrode during a cycle.

Note: The transformation process of the TMBQ@KMCN electrode during charging and discharging was explored by ex-situ FTIR (Figure S23). Since the carbonyl groups of TMBQ are the active sites for Zn^{2+} ion storage, the signal change of carbonyl group is especially concerned. As shown in Figure S23, upon discharge, the carbonyl peak at 1630 cm^{-1} gradually disappears and C=C peaks with stretching vibration at 1661 cm^{-1} become attenuated. The weakening of the carbonyl vibration during the discharge can be attributed to the conversion of –C=O into –C–O– anions after acceptance of electrons, which is simultaneously accompanied by cations insertion for coordination.[11] Moreover, the conjugated quinone ring undergoes a conversion to a π-conjugated benzene ring during the discharge process. Compared to the π-conjugated benzene ring, quinone structure exhibits two symmetric double bonds in the six-membered carbon ring, induce a larger dipole moment change of anti-symmetric stretching vibration, resulting in stronger FTIR absorption.[12] Upon charging, the FTIR peaks gradually restore to the pristine state, demonstrating the reversible redox of the carbonyl group as

well as the reversible transition of the conjugated structure.

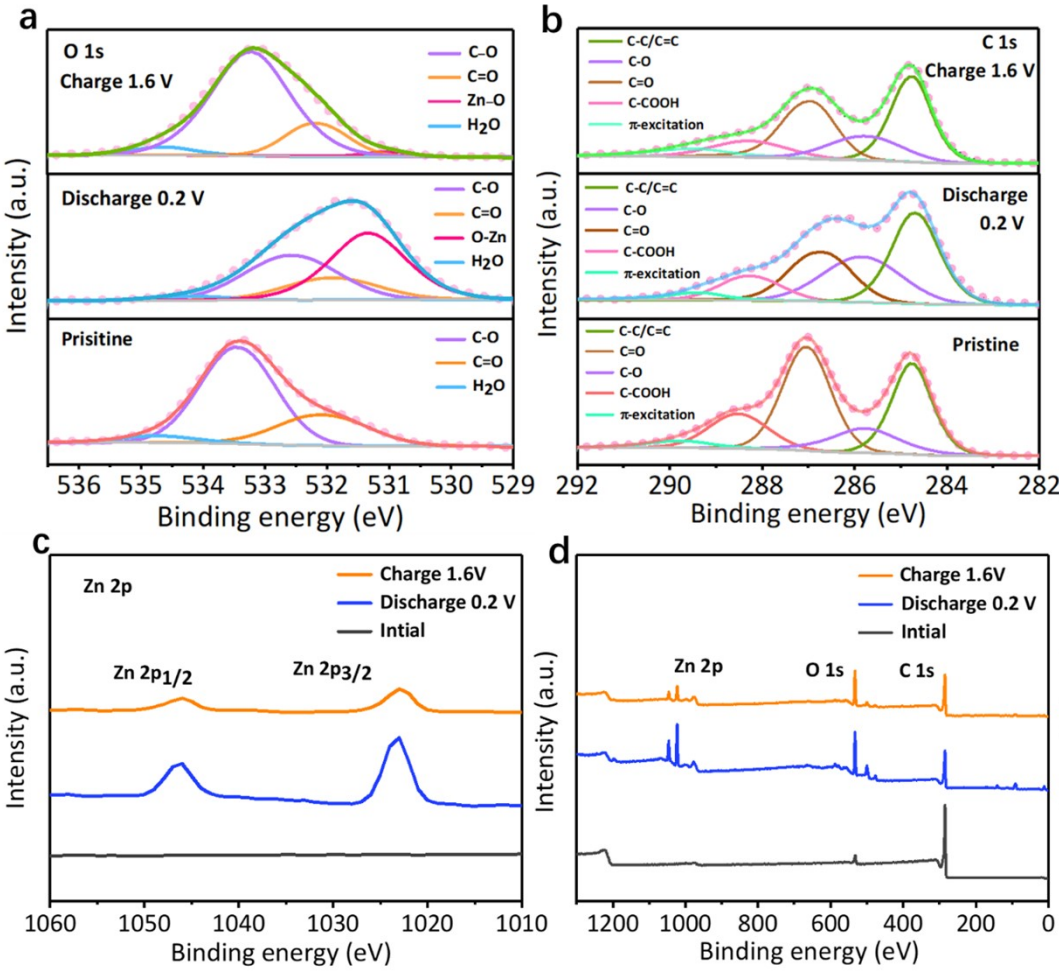

Figure S24. The high-resolution XPS spectra of O 1s (a), C 1s (b) and Zn 2p (c) spectra of the TMBQ@KMCN electrode at different charge/discharge voltages. (d) XPS survey spectra of the TMBQ@KMCN electrode at different charge/discharge voltages.

Note: To monitor the valence changes of O, C and Zn elements, the electrodes at fully charged or discharged state were investigated by ex-situ XPS test. Figure S24a demonstrates the high-resolution O 1s spectra, in which the –C=O peak (532 eV) became weak and a new peak of–O–Zn peak at 531 eV[13] came out at the fully

discharged state. When the electrode was recharged to 1.6 V, the –C=O peak went back to the initial state and the –O–Zn peak almost disappeared. Similarly, the –C=O bond in the high-resolution C 1s spectrum also got weakened and recovered upon charging and discharging (Figure S24b). For Zn 2p spectra shown in Figure S24c, the characteristic peak of Zn 2p is absent in the original TMBQ@KMCN electrode, but emerges with a strong intensity in the fully discharged state of 0.2 V, which is ascribed to constant insertion of Zn^{2+}ions into the TMBQ@KMCN. Moreover, the Zn 2p peak still remains but gets much weakened in a fully charged state of 1.6 V, due to that part of Zn^{2+} ions are captured by the TMBQ@KMCN during the discharging process. These results, together with the FTIR spectra, suggest the high reversibility of carbonyl group acts as active sites to coordinate with the Zn^{2+} in the charging and discharging process.

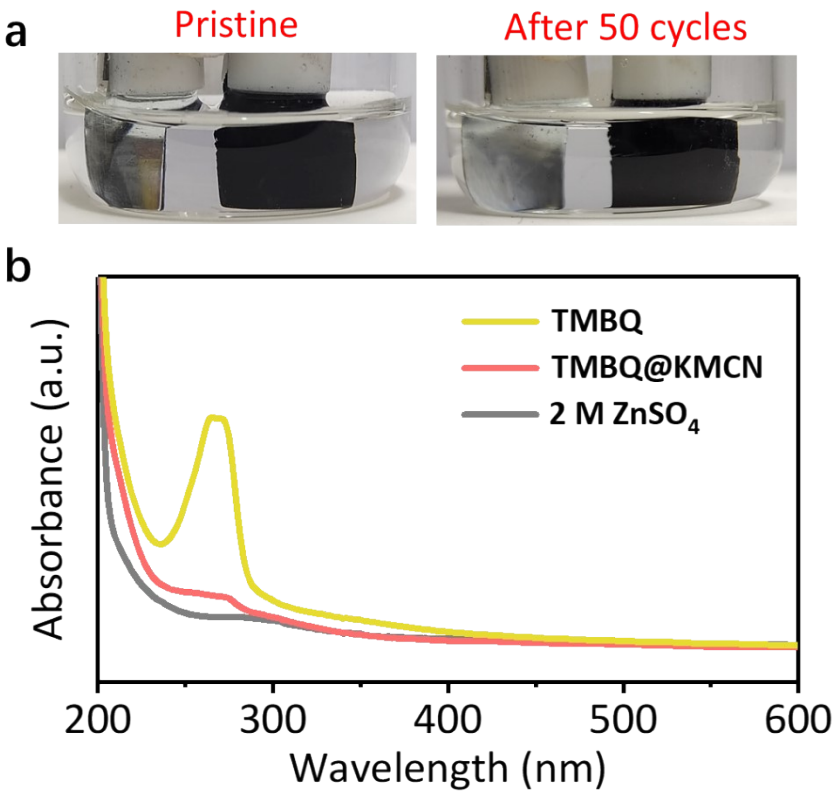

Figure S25. (a) Visual beaker cells based on the TMBQ@KMCN electrode prior to cycling and after 50 cycles at 5 C. (b) UV-vis spectra of the electrolyte of cells based on the TMBQ@KMCN and TMBQ electrode after 50 cycles.

Note: We investigate the dissolution of TMBQ during the charge and discharge process, and the electrolytes of the cells based on the TMBQ@KMCN and TMBQ electrode after 50 cycles were detected by UV-vis spectroscopy (Figure S25a). A notable absorption peak located at 260 nm appeared in the electrolyte of TMBQ electrode-based cell (Figure S25b), corresponding to the adsorption of n-π* and π-π* in the benzene structure of TMBQ,[14] indicating substantial dissolution of the reaction products of TMBQ after cycling. On the contrary, the TMBQ@KMCN electrode-based electrolyte showed almost no discernible difference in absorption peaks after cycling

compared to the initial electrolyte, evidently confirming the effective space-confined effect of KMCN that avoids the dissolution of discharging product of TMBQ.

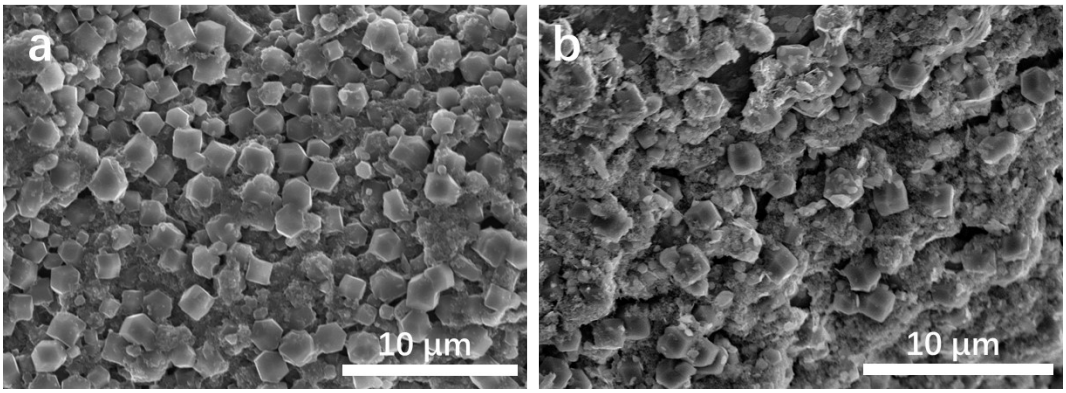

Figure S26. SEM images of the TMBQ@KMCN electrode before (a) and after 10000 cycles at 10 C (b).

Note: The SEM images of TMBQ@KMCN electrode after 10,000 cycles also reveal that no TMBQ with a fiber-like shape appears (Figure S26), further demonstrating that TMBQ or Zn-TMBQ is effectively confined within the pores of KMCN during cycling, and this result is also consistent with the UV-vis data.

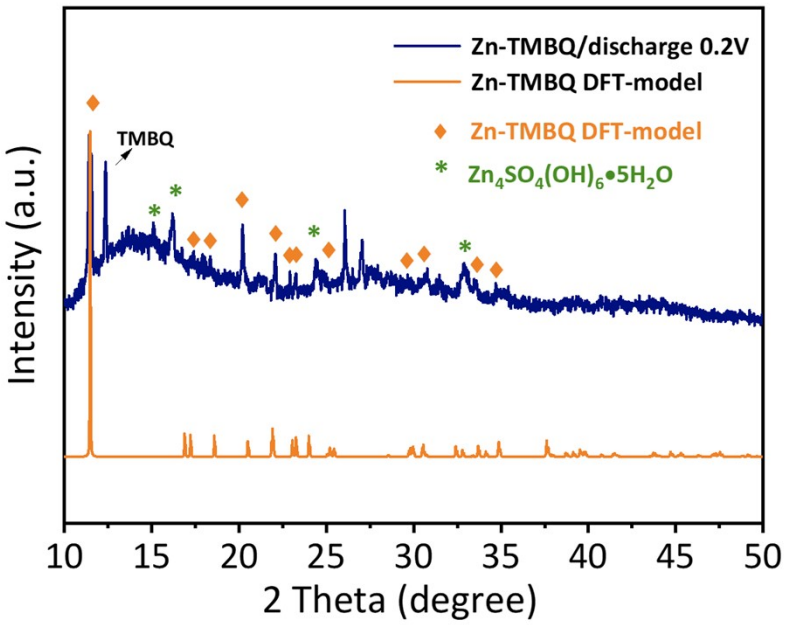

Figure S27. Comparison of the experimental XRD pattern of the fully discharged TMBQ (Zn-TMBQ, at a discharging voltage of 0.2 V) with the simulated model by DFT calculation.

Note: The reflection at around 12.5° in Figure S27 is attributed to TMBQ, which is possibly due to some TMBQ molecules not fully participating in the reaction process during the initial discharge cycle.

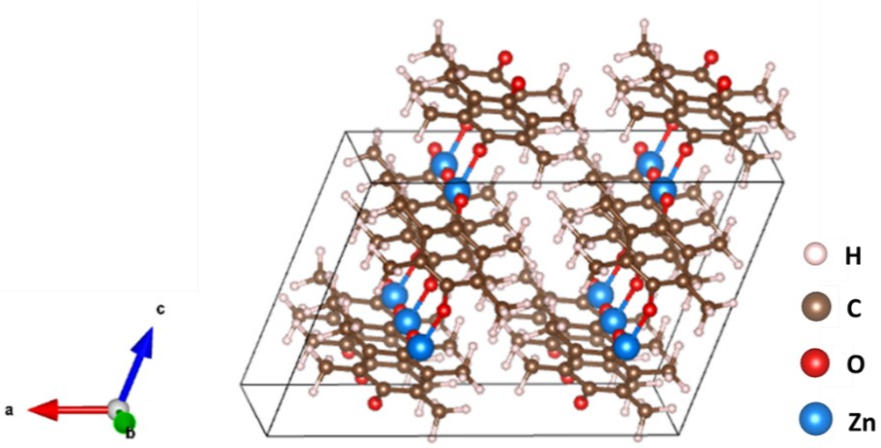

Figure S28. Structural model of Zn-TMBQ obtained from DFT structural optimization.

Note: The structure model of Zn-TMBQ corresponds to a state that Zn ions fully insert into TMBQ structure and coordinate with carbonyl groups of TMBQ, corresponding to a fully discharged state of 0.2 V.

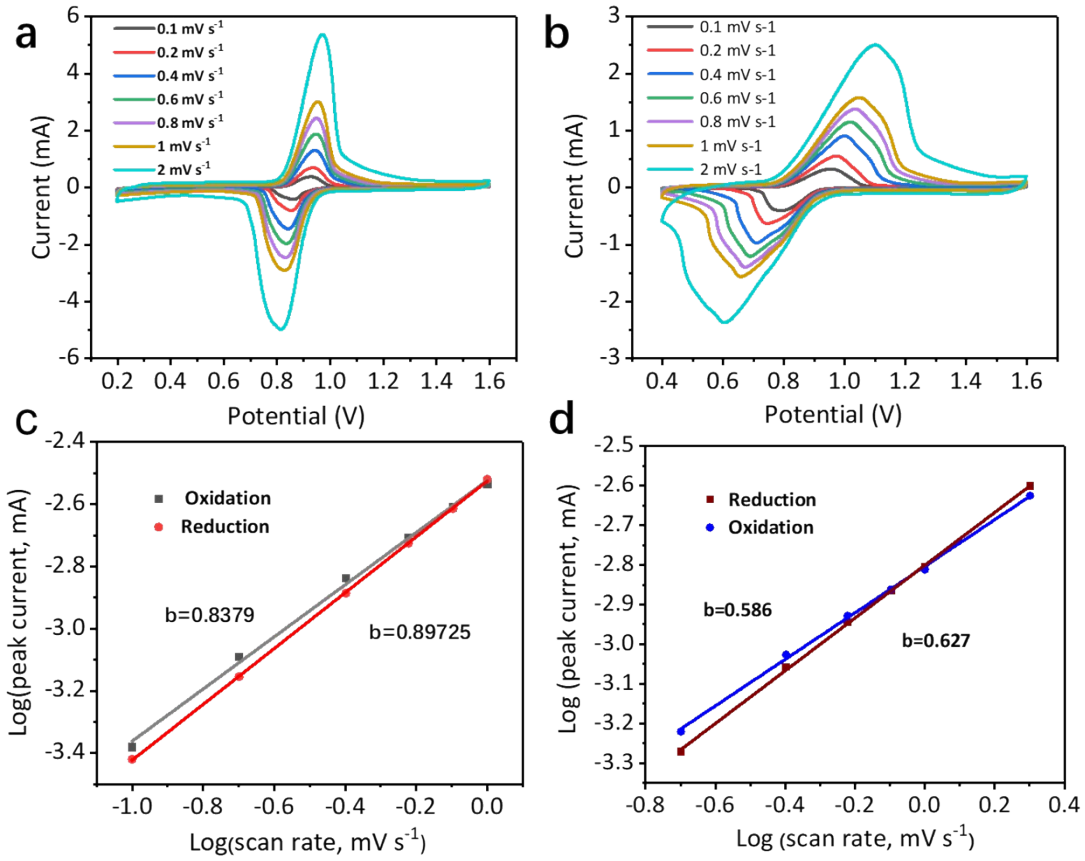

Figure S29. (a, b) CV curves at various scan rates from 0.1 to 2 mV s^{-1} of the TMBQ@KMCN and TMBQ electrode, respectively. (c, d) Logarithmic relationship of peak current with scan rate for the CV curves in (a) and (b), respectively.

Note: We analyzed the CV curves of the TMBQ@KMCN electrode collected at various sweep rates from 0.1 to 2.0 mV s^{-1}. As the sweep rate increases, the cathodic peak shifts to lower potentials and the anodic peak shifts to higher potentials, due to increased polarization. Compared to the TMBQ electrode, the polarization of the

TMBQ@KMCN electrode with increasing sweep speed is significantly smaller (Figure S29a, b). The percentage of capacitive contribution of a battery system can be qualitatively estimated from the CV curves based on the following equation:

$$i = av^b$$

Where i is the measured current, v refers to the scan rate of CV, a and *b* are adjustable values. *b* can be determined by the slope of the log(v)-log(i) plots. *b* value of 0.5 indicates that the current is controlled by semi-infinite diffusion (battery energy storage mechanism) while $b = 1$ indicates capacitive behavior (capacitive energy storage mechanism). The b value of the pure TMBQ electrode for both anodic and cathodic peaks are nearly 0.5, suggesting a predominantly diffusion-controlled kinetics for faradic Zn^{2+} storage in TMBQ (Figure S29d). But for the TMBQ@KMCN electrode, the b value for both anodic and cathodic peaks are around 0.85 (Figure S29c), which indicates a capacitive-dominated charge storage behavior. This finding suggests that capacitive processes dominate charge storage behavior in the TMBQ@KMCN system, due to the uniform dispersion and confinement of TMBQ in the porous KMCN, which is beneficial to superior rate capability as well as super cycling stability.

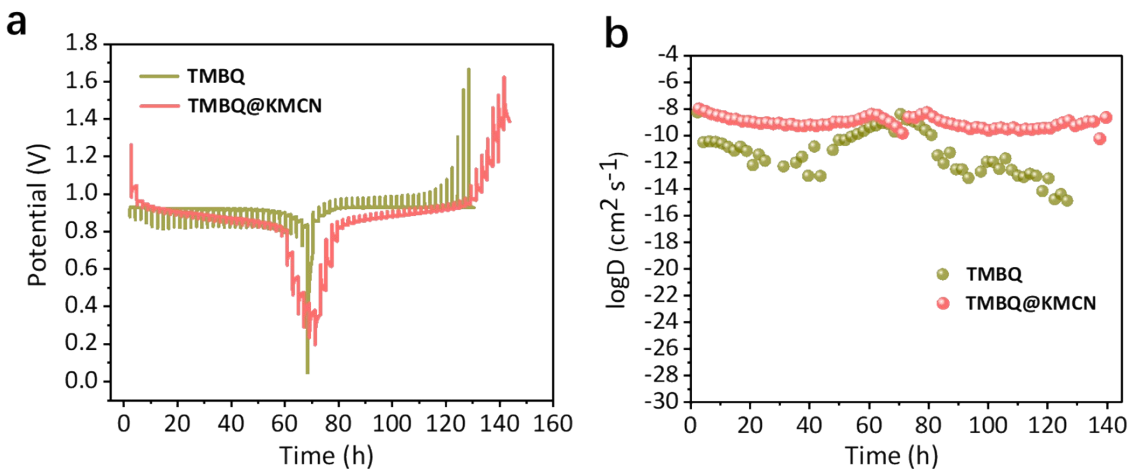

Figure S30. (a,b) GITT curves (a) and Zn^{2+} diffusion coefficient (b) of the TMBQ and TMBQ@KMCN electrodes.

Note: The zinc diffusion coefficient was measured by using galvanostatic intermittent titration technique (GITT) and calculated based on the equation:

$$D = \frac{4L^2}{\pi\tau}\left(\frac{\Delta E_S}{\Delta E_t}\right)^2$$

Where *t* is the duration of the current pulse (s), τ is the relaxation time (s), and Δ*Es* is the steady-state potential change (V) by the current pulse. ΔEτ is the transient voltage-change during a single titration step. L is zinc ion diffusion length (cm); for compact electrode, it is equal to thickness of electrode.

The diffusion coefficient varies at the course of discharge/charge, with the minima appearing at redox plateau (Figure S30), where the Zn^{2+} was deeply diffused into/from the TMBQ framework. The Zn^{2+} diffusion coefficient in the TMBQ@KMCN was obviously higher than that in TMBQ as a whole, suggesting ion-diffusion and conductivity enhancement over the TMBQ@KMCN electrode. Therefore, the TMBQ@KMCN interface imparts the electrode facilitated rate capability.

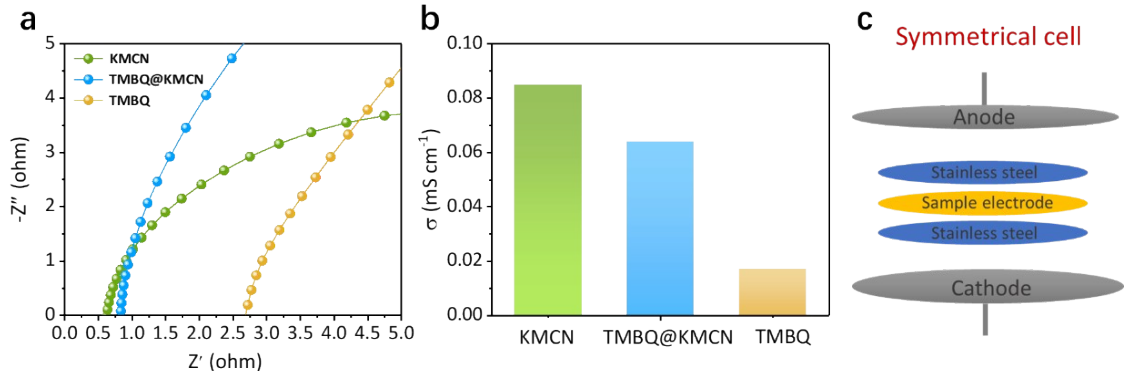

Figure S31. (a) Electrical impedance and (b) ionic conductivity of the TMBQ@KMCN, KMCN and TMBQ electrodes. (c) Schematic illustration of a symmetrical cell.

Note: Two stainless steels were used to place the TMBQ, KMCN, and TMBQ@KMCN separators to assemble into batteries. The ion conductivity was calculated according to the followingrelation equation:

$$\sigma = \frac{I}{R_b A}$$

where σ represents the ion conductivity, I signifes the thickness of the separator, R_b stands for the resistance, and A is the area of electrodes.

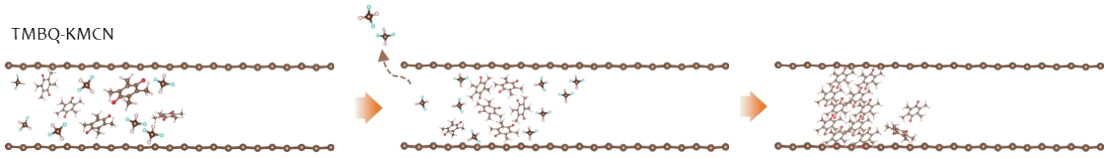

Figure S32. The crystallization process of TMBQ in saturated TMBQ-DCM solution impregnated without vacuuming.

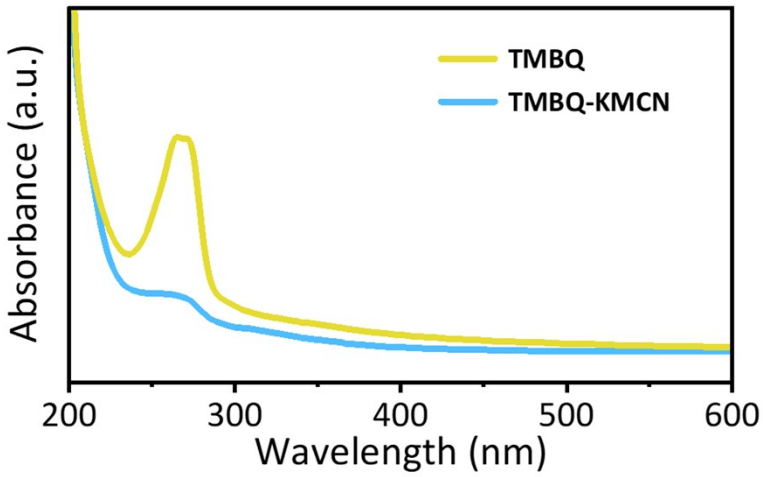

Figure S33. UV-vis spectra of the electrolyte of cells based on the TMBQ-KMCN and TMBQ electrode after 50 cycles.

Note: It can be found that the TMBQ-KMCN electrode-based electrolyte also shows almost no discernible difference in absorption peaks after cycling compared to the initial electrolyte, indicating that despite a low loading and limited pore depth of TMBQ impregnation in TMBQ-KMCN, the TMBQ molecules undergo the same crystallization process like that in TMBQ@KMCN, which exhibits effective space-confined effect of KMCN that avoids the dissolution of the discharging product of TMBQ.

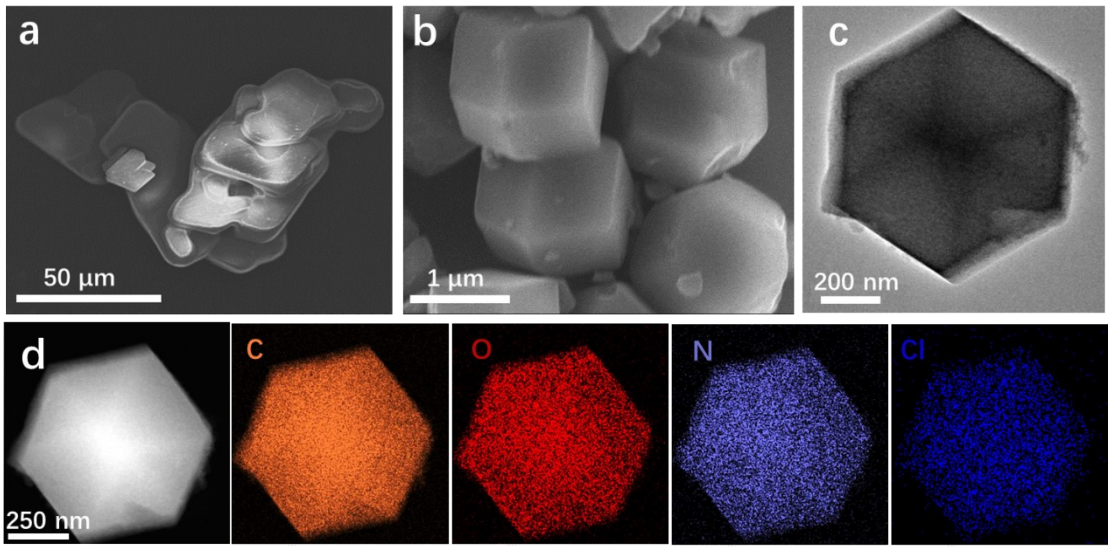

Figure S34. (a, b) SEM images of TCBQ (a) and TCBQ@KMCN (b). (c, d) TEM image (c) and EDX element mapping (d) of TCBQ@KMCN.

Note: The morphology of TCBQ@KMCN closely resembles that of KMCN, with no block-like structures attributed to TCBQ observed in its vicinity (Figure S34a-c). EDX elemental mapping analysis reveals a uniform distribution of chlorine, providing evidence for the homogeneous loading of TCBQ into KMCN (Figure S34d).

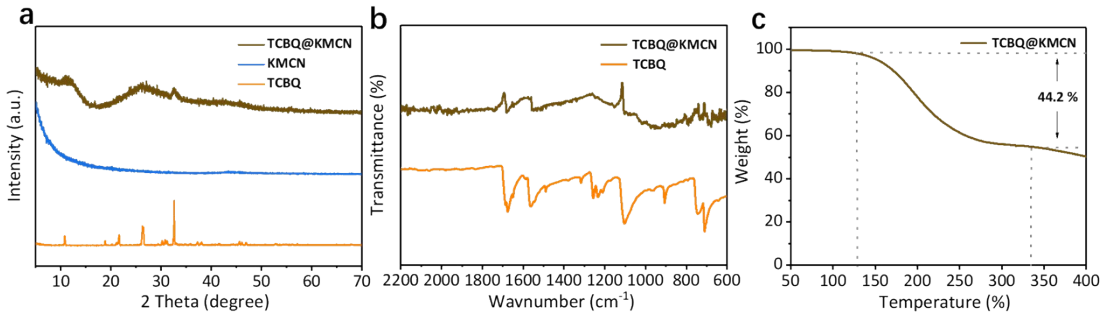

Figure S35. (a) XRD patterns of the TCBQ@KMCN, KMCN, TCBQ. (b) FTIR curves of the TCBQ@KMCN and TCBQ. (c) TGA curve of TCBQ@KMCN.

Note: In XRD patterns, the characteristic peaks of TCBQ exhibited a weakened, bulging pattern, similar to what was observed in the TMBQ@KMCN. FIRT curves revealed distinct peaks corresponding to C=O bonds after loading. Additionally, the TGA curve indicated an effective loading of TCBQ in KMCN is about 44.2%.

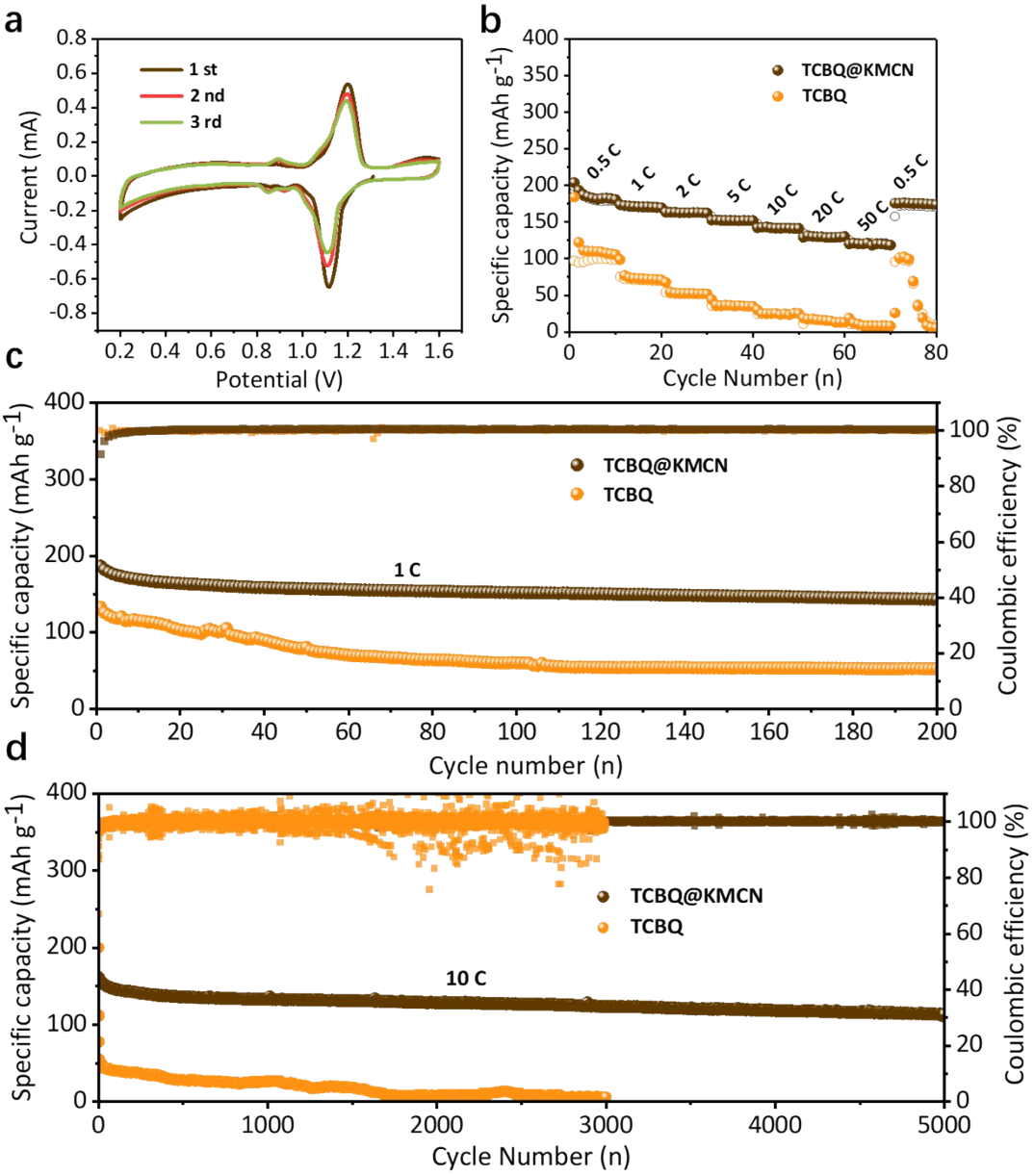

Figure S36. (a) CV curves of the TCBQ@KMCN electrode at 0.2 mV s^{-1}. (b) Rate capability of the TCBQ@KMCN electrode at current densities between 0.5 and 50 C. (c) Cycling performance of the TCBQ@KMCN electrode at 1 C. (d) Long cycling performance of the TCBQ@KMCN electrode at 10 C. Here 1 C = 218 mA g^{-1}.

Note: Due to the electron-withdrawing of the -Cl group, the reduction and oxidation peaks in the CV curves of TCBQ@KMCN (1.12 and 1.20 V, Figure S36a) are expected to be higher than those of the TMBQ@KMCN (Figure S10a).[26] Compared to pure TCBQ electrode, TCBQ@KMCN electrode exhibits outstanding rate capability (Figure S36b). The high reversible capacity of ≈ 192, 173, 164, 153, 143, 132, 122 mAh g^{-1} is achieved at 0.5, 1, 2, 5, 10, 20, and 50 C, respectively. When the current goes back to the initial 0.5 C after 70 cycles, a reversible capacity of 178 mAh g^{-1} can be maintained, giving a high capacity retention of 92.7%. Furthermore, the TCBQ@KMCN electrode also exhibits significantly enhanced cycling stability compared with the pure TCBQ electrode. When the TCBQ@KMCN electrode at a current density of 1 C, it can be found that the TCBQ@KMCN electrode retains a high capacity of 158 mAh g^{-1} and a Coulombic efficiency of 99.87% after 200 cycles (Figure S36c). When the current density is increased to 10 C, the TCBQ@KMCN electrode can still retains a specific capacity of 125 mAh g^{-1} after 5000 cycles (Figure S36d).

Table S1. Elemental content of the KMCN and TMBQ@KMCN.

Simple	C (wt%)	N (wt%)	O (wt%)
KMCN	88.02	6.96	5.02
TMBQ@KMCN	85.71	2.17	12.12

Table S2. Specific surface area and pore analyses of the typical KMCN and TMBQ@KMCN.

Simple	S_{BET} (m^2/g)	S_{mico} (m^2/g)	V_{total} (cm^3/g)	V_{mico} (cm^3/g)	$D_{average\ pore}$ (nm)
KMCN	3277.38	2950.05	2.62	1.77	3.23
TMBQ@KMCN	252.37	235.07	0.17	0.13	

Table S3. Comparison of rate capacity and cycling performance of recently reported organic molecule cathode materials based on carbonyl energy storage for ZIBs.

Simple	Rate Capacity (mAh g^{-1})	Long-cycle rate	Number	Capacity Retention (mAh g^{-1})	Refs.
TMBQ@	**155@48.9 A g^{-1} (150 C)**	6.52 A g^{-1} (20 C)	15000	211	This work
KMCN		16.3 A g^{-1} (50 C)	10000	178	This work
TCBQ-CMK-3	68@2.2 A g^{-1}	218 mA g^{-1} (1 C)	200	118	15
PQ@AC	91@20 A g^{-1}	5 A g^{-1}	36000	108	16
SQ/CMK-3	149@2 A g^{-1}	1 A g^{-1}	330	109	17
PT/CMK-3	92@20 A g^{-1}	2.5 A g^{-1}	5000	127	18
NQ@CNT	129@20 C	339 mA g^{-1} (1 C)	1500	137	19
DTT	97@2 A g^{-1}	10 A g^{-1}	23000	78	20
PQ-Δ	210@ 0.15 A g^{-1}	0.15 A g^{-1}	500	210	21
PTO	113@ 20 A g^{-1}	3 A g^{-1}	1000	145	22
PTONQ	140@35 A g^{-1}	10 A g^{-1}	10000	163	23
TABQ	213@5A g^{-1}	5 A g^{-1}	1000	200	24
TDT	182@10 A g^{-1}	10 A g^{-1}	3000	148	13

TABQ-PQ	139@20 A g^{-1}	5 A g^{-1}	30000	140	25
C4Q	172@ 1 A g^{-1}	0.5 A g^{-1}	1000	120	26
PCTB	80@8 A g^{-1}	3 A g^{-1}	4000	79	27
BDTD	64@ 30 A g^{-1}	5 A g^{-1}	10000	75	28
PMC	105@8 A g^{-1}	8 A g^{-1}	1000	69	29
NDI	120@1 C	201 mA g^{-1} (1 C)	1000	100	30
4S6Q	208@30 A g^{-1}	3 A g^{-1}	20000	240	31
PTA-O26	98@1.6 A g^{-1}	0.2 A g^{-1}	350	126	32
2PDI	41@8 A g^{-1}	3A g^{-1}	50000	46	33
2Cl-NQ	61@10 A g^{-1}	10 A g^{-1}	1000	41	34
AQ	N/A	0.2 A g^{-1}	200	146	35

Note: TCBQ, p-chloranil; NQ, naphthoquinone; SQ, seriniquinone; PQ, 9,10-phenanthraquinone; PQ-Δ, triangular macrocyclic phenanthrenequinone; PTO, pyrene-4, 5, 9, 10-tetraone; PMC, 3, 4, 9, 10-perylenetetracarboxylic dianhydride; PT, 5, 7, 12, 14-pentacenetetrone; NDI, 1, 4, 5, 8-naphthalene diimide; TABQ, tetraamino-p-benzoquinone; TDT, 2, 3, 7, 8-tetraamino-5, 10-dihydrophenazine-1, 4, 6, 9-tetraone; TABQ-PQ, dibenzo [a, c] dibenzo [5, 6: 7, 8] quinoxalino [2, 3-i] phenazine-10, 21-dione; 2PDI, perylene-based imide with expanding π-conjugated system; BDTD, benzo[1, 2-b: 4, 5-b']-dithiophene-4, 8-dione; DTT, dibenzo [b, i] thianthrene-5, 7, 12, 14-tetraone; PCTB, poly (2-chloro-3, 5, 6-trisulfde-1, 4-benzoquinone); 2Cl-NQ, 2, 3-

Cl-1, 4-naphthoquinone; AQ, 9, 10-anthraquinone.[13,15-35]

Table S4. Porosity parameters of the MCN and KOH-activated MCN samples.

Simple	S_{BET} (m^2/g)	S_{mico} (m^2/g)	V_{total} (cm^3/g)	V_{mico} (cm^3/g)	$D_{averagepore}$ (nm)
MCN	404.22	374.50	0.21	1.88	1.98
KMCN-L	3,212.53	1655.60	1.70	1.51	2.12
KMCN	3,277.38	2950.05	2.62	1.77	3.23
KMCN-H	3,894.09	1557.62	2.70	0.83	3.93

Note: After KOH activation, pore size of MCN was further enlarged, resulting in a richer KMCN pore structure. As the mass ratio of KOH: MCN increases, the total specific surface area and total pore volume of KMCN gradually rise, and at the same time, the percentage of mesopores inside KMCN gradually increases. The average pore size also increases from 2.12 nm to 3.93 nm.

Table S5. The crystal lattice parameters of TMBQ after Zn ions inserted.

Sample	a	b	c	alpha	beta	gamma	Unit-cell volume
TMBQ	8.51490	5.07509	9.56740	90.0534	108.6315	90.1381	391.8 Å^3
Zn-TMBQ	8.27635	4.77200	11.04763	90.0041	111.2578	90.1451	406.6 Å^3

Reference

1 G. Kresse and J. Furthmuller, *Comput. Mater. Sci.*, 1996, **6**, 15.

2 G. Kresse and J. Furthmüller, *Phys. Rev. B*, 1996, **54**, 11169.

3 J. P. Perdew, K. Burke and M. Ernzerhof, *Phys. Rev. Lett.*, 1998, **80**, 891.

4 G. Kresse and D. Joubert, *Phys. Rev. B*, 1999, **59**, 1758.

5 P. E. Blöchl, *Phys. Rev. B*, 1994, **50**, 17953.

6 S. Grimme, J. Antony, S. Ehrlich and H. Krieg, *J. Chem. Phys.*, 2010, **132**, 154104.

7 D. Rabinovich, G. Schmidt and E. Ubell, *J. Chem. Soc. (B)*, 1967, **131**.

8 G. Henkelman, B. P. Uberuaga and H. Jónsson, *J. Chem. Phys.*, 2000, **113**, 9901.

9 L. Wang, M. Peng, J. Chen, T. Hu, K. Yuan and Y. Chen, *Adv. Mater.*, 2022, **34**, 2203744.

10 X. Hu, J. Li, G. Zhong, Y. Liu, J. Yuan, S. Lei, H. Zhan and Z. J. S. Wen, *Small*, 2020, **16**, 2005534.

11 Z. Tie, L. Liu, S. Deng, D. Zhao and Z. Niu, *Angew. Chem. Int. Ed.*, 2020, **59**, 4920.

12 E. W. Zhao, T. Liu, E. Jonsson, J. Lee, I. Temprano, R. B. Jethwa, A. Wang, H. Smith, J. Carretero-Gonzalez, Q. Song and C. P. Grey, *Nature*, 2020, **579**, 224.

13 L. Lin, Z. Lin, J. Zhu, K. Wang, W. Wu, T. Qiu and X. Sun, *Energy Environ. Sci.*, 2023, **16**, 89.

14 X. Yang, Y. Ni, Y. Lu, Q. Zhang, J. Hou, G. Yang, X. Liu, W. Xie, Z. Yan, Q. Zhao and J. Chen, *Angew. Chem. Int. Ed.*, 2022, **61**, e202209642.

15 D. Kundu, P. Oberholzer, C. Glaros, A. Bouzid, E. Tervoort, A. Pasquarello and M. Niederberger, *Chem. Mater.*, 2018, **30**, 3874.

16 B. Yang, Y. Ma, D. Bin, H. Lu and Y. Xia, *ACS Appl. Mater. Interfaces*, 2021, **13**, 58818.

17 M. Zhang, C. Ding, C. Li, Y. Wang and W. Huang, *Sci. China Mater.*, 2023, **66**, 3104.

18 C. Mirle, V. Medabalmi and K. Ramanujam, *ACS Appl. Energy Mater.*, 2021, **4**, 1218.

19 J. Kumankuma-Sarpong, S. Tang, W. Guo and Y. Fu, *ACS Appl. Mater. Interfaces*, 2021, **13**, 4084.

20 Y. Wang, C. Wang, Z. Ni, Y. Gu, B. Wang, Z. Guo, Z. Wang, D. Bin, J. Ma and Y. Wang, *Adv. Mater.*, 2020, **32**, 2203744.

21 K. W. Nam, H. Kim, Y. Beldjoudi, T.-w. Kwon, D. J. Kim and J. F. Stoddart, *J. Am. Chem. Soc.*, 2020, **142**, 2541.

22 Z. Guo, Y. Ma, X. Dong, J. Huang, Y. Wang and Y. Xia, *Angew. Chem. Int. Ed.*,

2018, **57**, 11737.

23 T. Sun, Z. Yi, W. Zhang, Q. Nian, H. J. Fan and Z. Tao, *Adv. Funct. Mater.*, 2023, **8**, 2306675.

24 Z. Lin, H.-Y. Shi, L. Lin, X. Yang, W. Wu and X. Sun, *Nat. Commun.*, 2021, **12**, 4424.

25 T. Sun, W. Zhang, Z. Zha, M. Cheng, D. Li and Z. Tao, *Energy Storage Mater.*, 2023, **59**, 102778.

26 Q. Zhao, W. Huang, Z. Luo, L. Liu, Y. Lu, Y. Li, L. Li, J. Hu, H. Ma and J. Chen, *Sci. Adv.*, 2018, **4**, 1761.

27 Y. Zhang, C. Zhao, Z. Li, Y. Wang, L. Yan, J. Ma and Y. Wang, *Energy Storage Mater.*, **2022**, *52*, 386-394.

28 Z. Li, Y. Zhang, J. Xu and Y. Wang, *Batt. Supercaps,* 2022*,* **6***, e20220043.*

29 H. Zhang, Y. Fang, F. Yang, X. Liu and X. Lu, *Energy Environ. Sci.*, 2020, 13, 2515-2523.

30 M. Na, Y. Oh and H. R. Byon, *Chem. Mater.*, 2020, **32**, 6990.

31 T. Sun, W. Zhang, Q. Nian and Z. Tao, *Nano-Micro Letters*, 2023, **15**, 36.

32 X. Wang, G. Wang and X. He, *J. Colloid Interface Sci.*, 2023, **629**, 434.

33 L. Li, Y. Wang, W. Gong, M. Lin, L. Wei, Q. Li, Q. Zhang and L. Sun, *Chemical Engineering Journal*, 2023, **465**, 142824.

34 J. Wu, W. Xu, Y. Lin, X. Shi, F. Yang and X. Lu, *J. Power Sources.*, 2021, **483**, 229114.

35 Q. Wang, X. Xu, G. Yang, Y. Liu and X. Yao, *Chem. Commun.*, 2020, **56**, 11859.